JMEPEG
https://doi.org/10.1007/s11665-024-10099-0

1059-9495/$19.00

ORIGINAL RESEARCH ARTICLE

Investigating Optimum Hot Working Window of 2205 Duplex Stainless Steel Using Modified Dynamic Material Modeling

Elvis M. Gonya, Mamookho E. Makhatha, Charles W. Siyasiya, Ndumiso M. Silubane, and Ngeleshi M. Kibambe

Submitted: 15 September 2023 / Revised: 22 November 2023 / Accepted: 15 May 2024

This paper uses a modified dynamic material modeling (MDMM) suggested by Murty and Rao to develop processing maps (PM) of 2205 duplex stainless steels (DSS). Gleeble 1500D, a thermo-mechanical simulator was used to conduct single hit compression tests at a temperature between 850 and 1050 °C and strain rates of 0.001-5 s^{-1}. Additionally hot compression tests at a strain rate of 15 s^{-1} and same temperature range were also conducted on a Bahr 805 dilatometer. As per general procedure acquired stress-strain data were corrected for friction and adiabatic heating, before constructing PMs at true strains of 0.1, 0.3, 0.5 and 0.8. Microstructures to validate the PM were prepared from safe domains and instability regimes belonging to PM of 0.8 true strain. Results showed that hot processing at intermediate to high strain rates and temperature leads to formation of flow instabilities such as mechanical twins and adiabatic shear bands. Safe domain located within the temperature range of (850-925) °C, strain rates of (2.6-15) s^{-1} and peak η = 35% gave an inhomogeneous microstructure with presumably non-uniform mechanical properties. This region was considered ideal for hot processing of 2205 DSS provided that deformation conditions are carefully controlled to optimise DRX. Low Z conditions also provided an optimum hot working for hot processing.

Keywords 2205 duplex stainless steel, instability regimes, processing maps, safe domain

1. Introduction

Duplex stainless steels (DSS) are dual phase alloys that have earned several engineering applications due to their exceptional mechanical properties. Particularly, the excellent properties are attributed to the dual phase microstructure comprising of almost equal proportions of ferrite and austenite (Ref 1). In which, the alloy tends to have a combination of mechanical properties from the single phase austenitic and ferritic stainless steels (Ref 2, 3). In petroleum, refinery, and pulp and paper industries, shell structures of thick-walled cylindrical vessels (heat exchangers) are fabricated from plates or metal sheets of 2205 DSS. These plates or metal sheets are produced from hot rolling (HR), which is generally conducted at high speed and higher temperatures to take advantage of high production rate and lower rolling forces.

HR is a thermomechanical process (TMP) that involves the optimisation of process parameters (strain, strain rate and temperature) in order to initiate good restoration mechanisms (Ref 4). These mechanisms play a crucial role in refining the deformed structure to improve the mechanical properties of the final rolled products (Ref 5). On the other hand, their absence warrant poor mechanical properties and defective end product (Ref 6, 7). HR of DSS comes with significant challenges due to their poor hot workability, which often leads to edge cracking of the final rolled products (i.e., plates). According to Faccoli and Roberti (Ref 2), poor hot workability of DSS can be ascribed to difference in restoration behaviour between austenite and ferrite. For instance, Han et al. (Ref 1), explained that the manner in which each phase soften or restore in DSS is dependent on the magnitude of stacking faults energy (SFE). Their work (Ref 1), showed that non-conservative movement of dislocations was easier in ferritic phase due to high SFE and subsequently it restored by means of dynamic recovery (DRV). Whereas in austenitic phase, low SFE restricted the movement of partial dislocations to a specific slip system. Such that these dislocations pile up at any barriers of slip and accumulate to a level that is critical for initiation of dynamic recrystallization (DRX).

Studies from Qiannan et al. (Ref 8), Min et al. (Ref 7) and Zhao et al. (Ref 9), elaborated on the importance of DSS phase balance, where higher volume fraction of ferrite (softer phase) at elevated temperature was thought to be responsible for improved in hot workability of DSS. Apart from differences in restoration behavior and phase balance, other common causes of poor hot workability in DSS include differences in thermal expansion between the phases, presence of coherent interfaces

Elvis M. Gonya, Mamookho E. Makhatha, and **Ndumiso M. Silubane**, Department of Metallurgy, Faculty of Engineering and the Built Environment, University of Johannesburg, John Orr Building, Johannesburg 2028, South Africa; **Charles W. Siyasiya**, Department of Materials Science and Metallurgical Engineering, University of Pretoria, Hatfield 0028 Pretoria, South Africa; and **Ngeleshi M. Kibambe**, Center for Nanoengineering and Advanced Materials (CeNAM), School of Mining, Metallurgy, and Chemical Engineering, University of Johannesburg, Doornfontein Campus, Johannesburg 2028, South Africa. Contact e-mails: elvisg@uj.ac.za, emakhatha@uj.ac.za, and emakhatha@gmail.com.

Published online: 19 November 2024

that causes stress accumulation at the interphases due to restricted grain boundary sliding, non-uniform strain distribution between the phases, strength difference between the phases and poor control of hot processing parameters.

Significant amount of research has been conducted to try and mitigate the mentioned challenges associated with hot processing of DSS. To this end, processing maps (PMs) remain the robust metallurgical tool that is available for hot processing optimisation (Ref 10). PMs were developed by Kumar and Prasad (K-P) on the basis of dynamic material modeling (DMM) (Ref 5). And since their inception, they have been successfully applied to many hot deformation studies, that analyse the response of an alloy to imposed hot processing conditions. Chen et al. (Ref 6), Momeni et al. (Ref 11), and Ma et al. (Ref 12) investigated the hot behaviour of 2205 DSS and suggested low strain rates and high temperatures (low Z conditions) as favourable conditions for hot processing. Using Prasad's instability criteria they (Ref 6, 11, 12) identified unsafe hot working zones at higher strain rates and temperature. In similar vein, Han et al. (Ref 13) studied the hot workability of 21 Cr as cast DSS, and also establish similar processing conditions (low strain rates and high temperatures). However, unsafe hot working zones were identified using two instability criteria which were K-P and Murty and Rao (M-R), where the latter was found to be the most reliable (Ref 13). There are very few studies that adopt M-R approach when investigating the general hot behavior of alloys. On this basis this paper seeks to use M-R approach in identifying good combination of process parameters that are suitable for hot processing.

2. Processing Maps

2.1 Background to Processing Maps

During hot rolling of metals and alloys, the expectation is to at least produce a quality sound rolled product with desired mechanical properties (Ref 14, 15). Such expectations can only materialise when the hot rolling mill operates within the optimum range. Where the deformation conditions (strain, strain rate and temperature) are carefully controlled to eliminate microstructural instabilities and promote good restorative mechanism (DRV, DRX and super-plasticity) (Ref 16, 17). The overall function of the restorative mechanisms is to improve the mechanical properties of the rolled product through microstructural refinement (Ref 18-20). In addition, minimal hot rolling loads are realised when restorative mechanisms such as DRX are at play and which this benefit the industrial hot mill to operate at lower energy costs (Ref 21, 22). In hot compression studies, restorative mechanisms are realised through flow curves, however this often creates challenges as some microstructural instabilities mimic these mechanisms. For example, the drop in flow stress post peak point is generally associated with softening of the material through DRX (Ref 23-25). Similarly, adiabatic heating or flow localisation also cause flow softening during hot deformation thus making it difficult to distinguish between good and unwanted deformation mechanisms. This challenge is often resolved by using processing maps that have a capability to make a clear distinction between good restorative mechanisms and flow instabilities.

As stated in the introduction, the processing maps were developed by Kumar and Prasad (Ref 5, 26) on the basis of dynamic material modeling (DMM) which applies the principles of continuum mechanics. In short, DMM explicitly explains the response of the deforming material to macroscopic deformation conditions (strain, strain rate and temperature) (Ref 27]. During hot working, the DMM specify that the deforming tools generate and transmit power to deforming specimen (Ref 28). Wherein the specimen act as a dissipator and allocate a significant portion of power towards raising its temperature while the rest is used for microstructural development through DRX and DRV (Ref 29-31). In mathematical form, the division of power is normally express in the following form (Ref 31):

$$P = \boldsymbol{\sigma}\dot{\boldsymbol{\varepsilon}} = G + J = \int_0^{\dot{\varepsilon}} \sigma d\dot{\varepsilon} + \int_0^{\sigma} \dot{\varepsilon} d\sigma \qquad \text{(Eq 1)}$$

where P = power, $\dot{\varepsilon}$ = strain rate (s^{-1}), σ = flow stress (MPa), G = G-content representing fraction of power that goes towards temperature rise and J = J-co content representing fraction of power given to microstructural development.

The manner in which power is distributed between the G and J depends on the strain rate sensitivity index (m) which gauges how the material in terms of flow stress respond to changes in strain rate (Ref 32). At low temperatures m is very low indicating no significant change in flow stress with change in strain rate (Ref 33]. However, with increase in temperature to a level of hot working, m-values increases and a noticeable change in flow stress is expected when strain rates are varied. The m-values are generally calculated from the slope of flow stress against the strain rate at constant strain and temperature (Ref 34):

$$\text{Strain rate sensitivity (m)} = \frac{\mathrm{d}(ln\sigma)}{\mathrm{d}(ln\dot{\varepsilon})} \qquad \text{(Eq 2)}$$

In turn, the m-values become an input in calculating the percentage of power allocated to microstructural changes. Such percentage as described by K-P is termed power dissipation efficiency and calculated by the following equation (Ref 35-37):

$$\eta_{K-P} = \frac{2m}{m+1} \qquad \text{(Eq 3)}$$

where η_{K-P}= power dissipation efficiency that measures the rate which the microstructure is being developed by DRX or DRV during hot working).

η values varies with deformation conditions and can be portrayed through a power dissipation efficiency (PDE) map which is a plot of temperature vs logarithmic strain rate at constant true strain. PDE map identifies the regions of high and low efficiencies during hot working. For instance, high η values are taken as indication that good softening mechanisms (e.g., DRV, DRX and super-plasticity) have occurred at a specific deformation conditions (Ref 38-40). Whereas low η values are generally associated with unwanted microstructural instabilities (i.e., adiabatic shear bands, flow localisation, dynamic strain aging, micro-cracks etc.,) (Ref 35). However, Feng et al. (Ref 41] and Quan et al. (Ref 42] cautioned that high η values do not necessarily mean good softening mechanisms, in some instances they may be associated with cracking of the material. In view of this, K-P (Ref 10) applied extremum principles of thermodynamics to define a useful parameter for identification of flow instabilities as follows (Ref 43):

$$\xi_{K-P}(\dot{\varepsilon}, T) = \frac{\mathrm{d}\ln\left[\frac{\mathrm{m}}{(\mathrm{m}+1)}\right]}{\mathrm{d}ln\dot{\varepsilon}} + m \leq 0 \qquad \text{(Eq 4)}$$

where ξ_{K-P} = instability coefficient and define the unsafe hot working zones where plastic flow of deforming alloy has been exceeded at the particular region.

Similarly, ξ values varies with deformation conditions at constant strain and can be represented on a plot of temperature vs logarithmic strain rate to produce an instability map. By placing this map on top of PDE map, a processing map is produced which clearly isolates the optimum zones of hot working from the instability regimes (Ref 36, 43, 44). K-P developed the DMM on the basis that the deforming alloy obeys power law and strain rate sensitivity remain constant (Ref 44, 45). However, several scholars (Ref 5, 46-48) have argued that while power law is valid for pure metals or low alloys systems, it is not applicable for complex alloys where m changes with both temperature and strain rate. In essence, the DMM may bring some errors when dealing with complex systems or high stress applications (Ref 48, 49). In response to constructive criticisms from several hot deformation studies, Murty and Rao (Ref 46) modified the DMM model to cater for complex alloy systems and all types of flow curves. Their work, (Ref 46) showed that the power dissipation efficiency can be calculated as follows:

$$\eta_{M-R} = 2\left(1 - \frac{1}{\sigma\dot{\varepsilon}}\left[\left(\frac{\sigma\dot{\varepsilon}}{m+1}\right)_{\dot{\varepsilon}=0.001} + \int_{0.001}^{\dot{\varepsilon}} \sigma \mathrm{d}\dot{\varepsilon}\right]\right) \qquad \text{(Eq 5)}$$

In terms of instability, Neethu and Chakravarthy (Ref 45) and Zhang et al. (Ref 50) also argued that the first term in (Eq 4) given as $\mathrm{d}ln\left[\frac{m}{(m+1)}\right]$ should be zero after differentiation, given that m is a constant. This implies that the instability criteria according to K-P should be $\xi = m < 0$. However, where m fluctuates with deformation parameters a different approach for computing the instability was defined by Murty and Rao (Ref 46) as follows:

$$\xi_{M-R} = 2m - \eta \qquad \text{(Eq 6)}$$

where instability occur when: $2\mathrm{m} - \eta < 0$

Till date there has been very few studies that compare Murty's and Prasad's approach (Ref 13, 44, 51). In terms of instability regimes, the findings from these studies (Ref 13, 44, 51), revealed that Murty's criteria predicts similar but narrower instability regions as compared to Prasad's criteria. In hot deformation studies of 2205 DSS, Prasad's approach had been popular when designing processing maps, probably due its simplicity. For instance, Fig. 1 illustrates processing maps of 2205 DSS constructed by Li et al. (Ref 8) and Chen et al. (Ref 6) at a true strain of 0.8 and 1.0 respectively. The chosen deformation parameters in each study were slightly different in terms range selected, however the instability regions (shaded areas) were almost similar and located at medium to high strain rates and temperatures between 1223 and 1350K and just above 1400K. Furthermore, both studies showed a peak efficiency of approximately 50% at low Z conditions.

3. Microstructural Features of Restoration Mechanisms

As alluded earlier in Sect. 2.1, the DRX and DRV are the most critical softening mechanisms during hot working of metal and alloys. The occurrence of these mechanisms could easily be identified through flow curves, where DRV normally maintain constant flow stress post peak stress while a drop in flow stress after a peak till attainment of steady state is associated with DRX as represented in Fig. 2 below (Ref 52).

To ascertain the occurrence of DRV or DRX during hot working, flow curves must be supported with microstructural analysis to confirm the type of restorative mechanism that dominated during hot working. According to Huang and Loge (Ref 53), the process of DRX can occur in three forms namely: (1) discontinuous dynamic recrystallisation (DDRX), (2) continuous dynamic recrystallisation (CDRX) and (3) geometric dynamic recrystallisation (GDRX). The latter process (GDRX) has been deemed to occur at higher strains ranging between 5 and 10, and since this range of strain was far higher than the one applied in this study the focus was the directed to the other two processes. The DDRX and CDRX processes can be briefly explain using Fig. 3 and 4 that were adopted from the study of Dong et al. (Ref 54).

3.1 Discontinuous Dynamic Recrystallization (DDRX)

During hot rolling of polycrystalline materials, any two adjacent grains may experience different amount strain because their orientation with respect to the working stress is not the same. As a result of strain variation from one grain to the other, the concentration of lattice defects generated and stored in each grain is different. Lattice defects such as dislocations are associated with elastic strain energy, which means their presence raises the stored energy of the deformed grain. And since the two adjacent grains are deforming differently, the amount of energy stored in each is not the same. Which lead to a differential energy that serves as the driving force to a process known as strain induced grain boundary migration (SIBM) (Ref 55). The SIBM has been regarded in many hot deformation studies as the responsible mechanism for the formation of new recrystallised grains in low stacking fault materials (Ref 56-59). As shown in Fig. 3, during SIBM, part of the original high angle boundary separating grain A and B bulges towards a higher energy grain via grain boundary migration (GBM). As the bulging continue, it drags a dislocation structure that re-arrange itself to form a subgrain adjacent to lower energy grain. In turn, the subgrain convert to high angle grain boundary through absorption of dislocations resulting in a formation of new DDRxed grain. The end result of an SIBM process is the necklace structure of fine DRXed grains that engulfed the entire high angle grain boundary and subsequently cover the entire original microstructure. Chen et al. (Ref 57) and Haghdadi et al. (Ref 58) have argued that the austenitic phase in DSS tends to soften by means of CDRX instead of DDRX due to limited number of austenite/austenite high angle boundaries that support the latter process. However, in another study of 2205 DSS, Haghdadi et al., (Ref 60) confirmed that limited DDRX may occur in this alloy, provided there are some distorted special high angle grain boundaries.

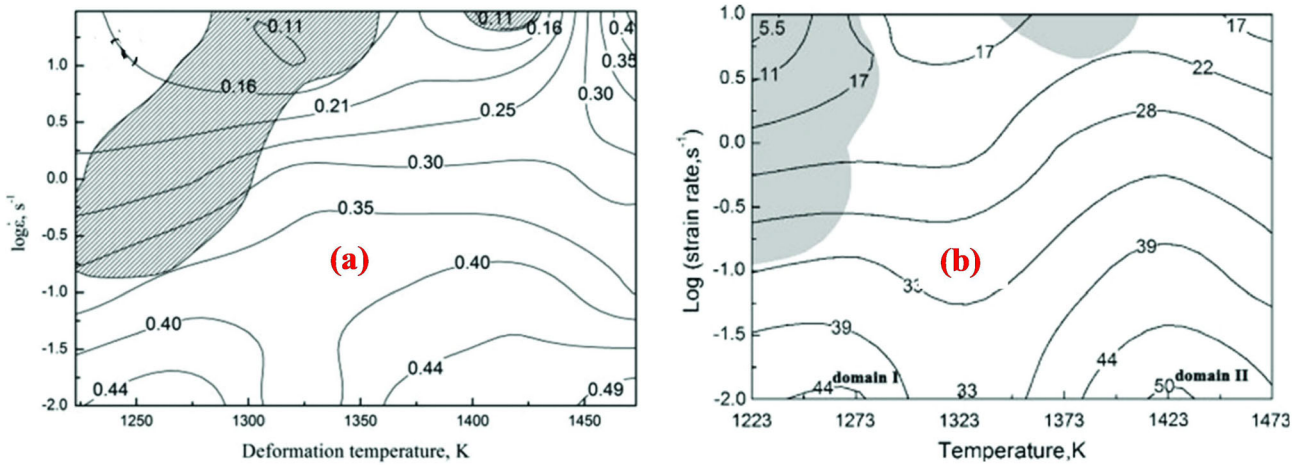

Fig. 1 (a) and (b) shows 2205 DSS PM constructed at 0.8 and 1.0 true strain respectively (Ref 16). Reprinted from *Materials & Design*, Vol 32, Lei Chen, Xiaocong Ma, Xiao Liu, Longmei Wang, Processing map for hot working characteristics of a wrought 2205 duplex stainless steel, Pages No. 1292-1297, Copyright 2011, with permission from Elsevier

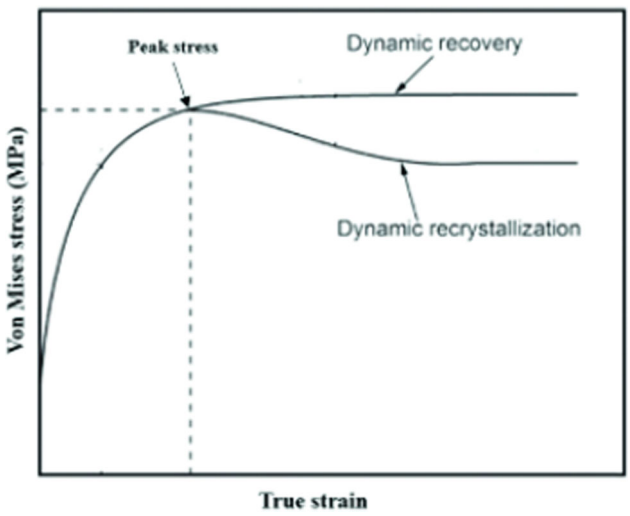

Fig. 2 Typical flow curve showing DRV and DRX behaviour (Ref 52)

3.2 Continuous Dynamic Recrystallisation (CDRX)

Unlike DDRX, the CDRX has been observed in materials of high SFE such as ferritic stainless steel, aluminium etc. The process of CDRX as shown in Fig. 4 occurs my means of subgrain rotation, initially the generated dislocations from plastic deformation glide and climb to form low angle subgrains (cell substructures) inside an original deformed grain. The adjacent subgrains then rotate, coalesce, and form a CDRXed grain.

During hot deformation studies, the occurrence of DDRX in low SFE materials is generally recognised through formation of necklace structure, serrated and bulging of boundaries(Ref 52, 61-63). Whereas visible high angle grain boundary that can be resolved by optical microscopy (OM) signify the occurrence of CDRX which is sometimes termed extended DRV. In instances whereby only DRV was active, the microstructure usually reveals subgrains within the deformed grain. Fig. 5 below was taken from the hot deformation study conducted by Chen et al. (Ref 16) in 2205 DSS, where the evolution of hot deformation structure through both DRX and DRV was observed. Fig. 5(f) showed fine DRXed grains of austenite dispersed around the ferrite-ferrite boundaries as well distinguishable high angle boundaries of ferrite which signified the occurrence DRV. The similar findings were also observed by Momeni and Dehghani (Ref 64), in a study of 2205 DSS, where well-developed grain boundaries on the ferrite matrix were attributed to DRV, while sub-boundaries such as deformation twins, bands on the austenite islands suggested the occurrence of DRX.

4. Experimental Procedure

The 16 mm rod of 2205 DSS acquired from Multi-alloys (LTD) in the as rolled condition was used to investigate the hot behaviour. Chemical composition of the alloy was confirmed through spectro analysis and the results in (wt.%) are displayed in Table 1 below. Furthermore, the as-received microstructure (Fig. 6) revealed a dual phase of ferrite matrix (brown) with austenite islands (light phase) oriented along the working direction.

4.1 Gleeble Hot Compression Tests

To analyse the hot deformation behaviour, twenty-five (25) cylindrical samples of 10 mm Ø × 15 mm height in size were prepared using wire cutting machine. After sectioning, each sample was prepared for Gleeble test as illustrated in Fig. 7. The hot deformation cycle as per Fig. 8 was programmed into the computer attached to the Gleeble unit, and hot processing conditions varied from sample to sample (*S1, S2*…, S25) during testing. All 25 samples were hot compressed in a Gleeble 1500D thermo-mechanical simulator to a total true strain of 0.8. The deformed structure was retained by fast cooling from the deformation to room temperature using helium. In addition to 25 samples, an extra five (5) cylindrical samples of 5 mm Ø × 10 mm height in size were also prepared and hot compressed in a Bahr 805 dilatometer at the same temperature range but higher strain rate of 15 s^{-1}.

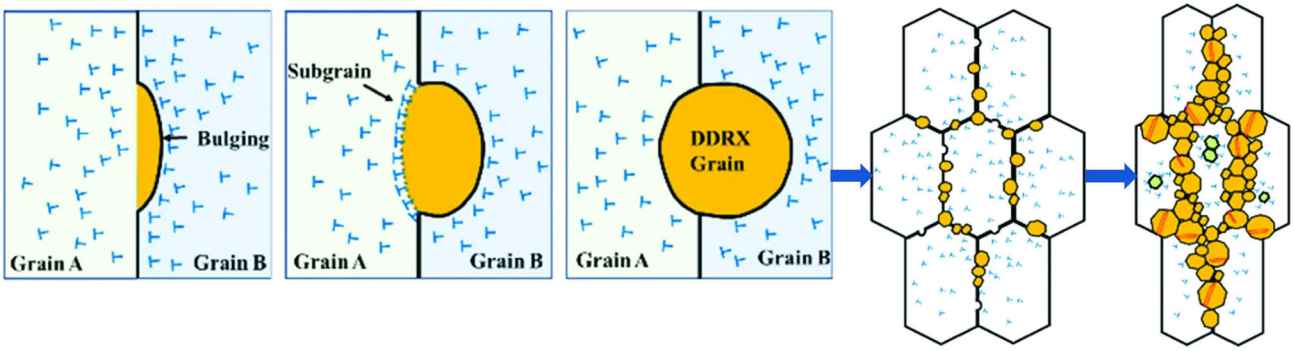

Fig. 3 Formation of necklace structure by DDRX through SIBM. Reprinted with permission from Springer Nature (Ref 54)

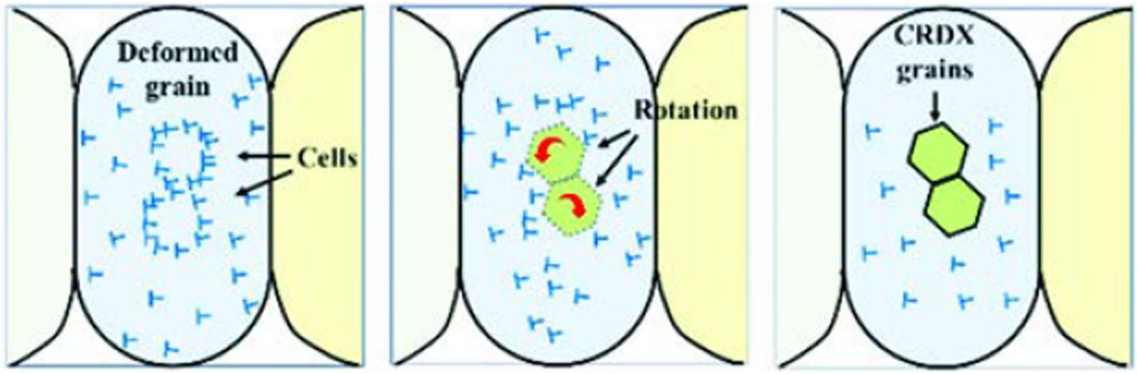

Fig. 4 Formation of CDRXed grain through sub-grain rotation. Reprinted with permission from Springer Nature (Ref 54)

4.2 Microstructural Preparation

The deformed samples of interest were sectioned in the middle parallel to the hot compression axis, mounted, ground to 1200 in grit size and polished down to 1 μm in diamond paste. Polished samples were then electro-etch at 2 V for 20 s with 60% nitric (HNO_3) solution. During compression, most deformation is concentrated at the center of the sample, thus optical and SEM images from the polished samples were taken around this region using optical microscope (OM) and high-resolution scanning electron microscope (HRSEM) respectively. The preparation of the microstructures was done to validate the safe domains and instability regimes of the developed processing maps.

4.3 Modification of Experimental Flow Curves

Post compression tests, the obtained flow curves may be affected by both friction and adiabatic heating. In the case of friction, flow stress values are usually higher than actual values whereas adiabatic heating due to higher strain rates may cause a reduction in flow stress values. To produce reliable constitutive analysis and processing maps experimental flow curves must be adjusted for both friction and adiabatic heating (Ref 65, 66).

4.3.1 Adjustment for Friction. During compression tests, a test-specimen normally changes its shape from a cylindrical to barrelled shape due to presence of friction. The degree of barrelling experienced by the deforming sample can be quantified through the barrelling factor (BF), to assess whether friction have any influence on the applied flow stress (Ref 65, 67, 68). According to Gong et al. (Ref 30), a BF $>$ 1.1 means that the frictional stress has a noticeable effect on the applied flow stress, and the latter will appear higher than expected values. Under this circumstance, flow curves from the laboratory experiments must be corrected for friction. In this study, barrelling factors at various deformation conditions were calculated by first taking the measurements of the barrelled samples as shown in Fig. 9 and plugged them into (Eq 7) to obtain the results given in Table 2 below. The results were extracted from temperatures of 900, 950 and 1000 °C for illustration purposes.

$$B = \frac{H_f R_M^2}{H_o R_0^2} \quad \text{(Eq 7)}$$

where $R_M^2 and H_f$ is maximum radius and final height after deformation respectively, and $H_o and R_0^2$ are initial height and radius.

Table 2 results showed that the deforming samples experienced significant friction between 900 and 950 °C, and as such flow curves belonging to these temperatures were adjusted for friction as shown in Fig. 10. Correction for flow curves belonging to 1000 °C was not necessarily due to BF $<$ 1.1. The correction was done by converting the Gleeble force and stroke data to Von Mises stress using (Eq 8) which considers the effect friction at the interface (between test specimen and tantalum foils).

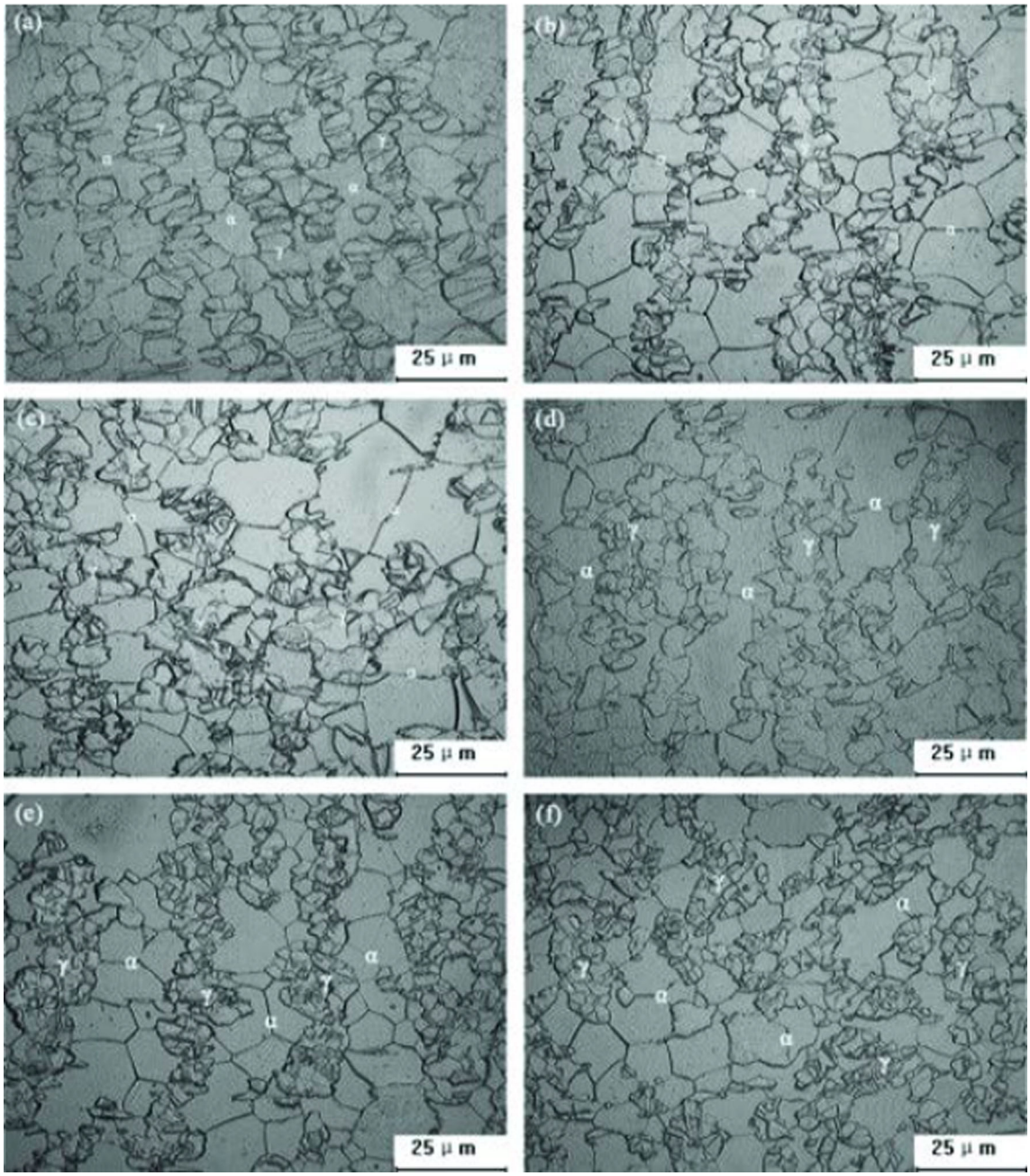

Fig. 5 Deformed microstructure at different conditions: (a) 1223 K /10 s^{-1}, (b) 1273 K/10 s^{-1}, (c) 1323/0.01 s^{-1}, (d) 1373 k/10 s^{-1}, (e) 1423 K/10 s^{-1}, and (f) 1473/0.01 s^{-1} (Ref 16). Reprinted from *Materials & Design*, Vol 32, Lei Chen, Xiaocong Ma, Xiao Liu, Longmei Wang, Processing map for hot working characteristics of a wrought 2205 duplex stainless steel, Pages No. 1292-1297, Copyright 2011, with permission from Elsevier

Table 1 2205 DSS chemical composition

%C	%Si	%Mn	%P	%S	%Cr	%Ni	%Mo	%N	%Fe
0.023	0.34	1.67	0.029	0.003	22.80	5.20	3.20	0.1703	66.57

$$\sigma_{\text{corr}-\text{flow stress}} = \frac{0.0625 P_x \mu^2 h_x^{-2}}{e^{\mu\sqrt{\left(d_o^2 h_o/h_x\right)}/h_x} - \mu\sqrt{\left(d_o^2 h_o/h_x\right)}/h_x - 1} \quad \text{(Eq 8)}$$

where: P_x = Gleeble force (in kN), h_x = stroke (in mm), d_0 = initial diameter (in mm), h_o = initial height (in mm), and μ = coefficient of friction at the interface and taken as 0.2

4.3.2 Adjustment for Adiabatic Heating. When conducting isothermal hot compression tests, one of the objectives is to maintain the constant temperature throughout the deformation process. This means that, the actual temperature measured by thermocouple should more or less match the set temperature. However, this is often hard to achieve when higher strain rates are applied during testing (Ref 70). The reason for this is that higher strain rates are coupled with shorter deformation times, thereby restricting the heat exchange between the deforming sample and the surroundings. Therefore, the actual temperature given by the thermocouple tends to be higher than the set one since the sample is not efficiently giving away heat, and isothermal conditions are not maintained (Ref 50). From the theory of thermodynamics, the inability of the system to adequately exchange heat with the environment is termed adiabatic heating. Similarly, failure of the deforming sample to successfully exchange heat with deformation tools (dies) during hot compression test is termed adiabatic heating (Ref 65).

Under adiabatic conditions, the sample temperature increases due to accumulation of heat causing deformation to occur at low flow stress values (Ref 71). This implies that, flow curves belonging to sample (s) that suffered from localised heating reflect lesser deformation resistance of the sample to applied stress. During the course of this study, the effect of adiabatic heating was first assessed by comparing the set temperature with that measured by the k-type thermocouple as shown in Fig. 11. The comparison showed no significant temperature difference between the strain rates of 0.001-0.1 s^{-1}. This was because low strain rates had longer deformation times that allowed the sample to adequately release heat to the surroundings such that equilibrium conditions were maintained. Consequently, the temperatures measured by the thermocouple did not deviate much from the set temperature (Ref 72).

However, for strain rates of 1, 5 and 15 s^{-1} the deviation from the set temperature averaged to 20 and 10 °C between 850 and 900 and 1050 °C respectively. Significant deviation at lower temperature was thought to be the increased in applied flow stress that subsequently raised the store strain energy of the sample. A similar observation was observed by Zhang et al. (Ref 70), Matsumoto and Chiba (Ref 71) and Lu et al. (Ref 34), where they attributed larger ΔT to (1) inability of the material to efficiently release heat at higher strain rates due to shorter deformation times, (2) larger applied stress at low deformation temperatures and (3) low specific heat capacity at low temperatures. Another noticeable deviation was at 1050 °C and strain rates of 0.1 and 1 s^{-1}, where the actual temperature fell below the desired temperature. This scenario was also observed by Qian et al. (Ref 72) and Wang et al., (Ref 73) and

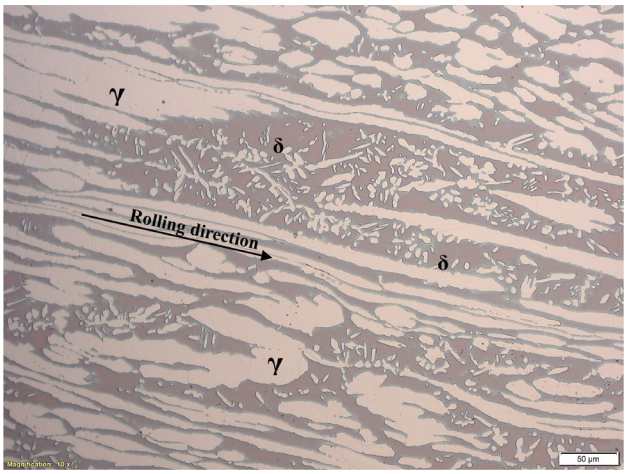

Fig. 6 As-received microstructure of 2205 DSS

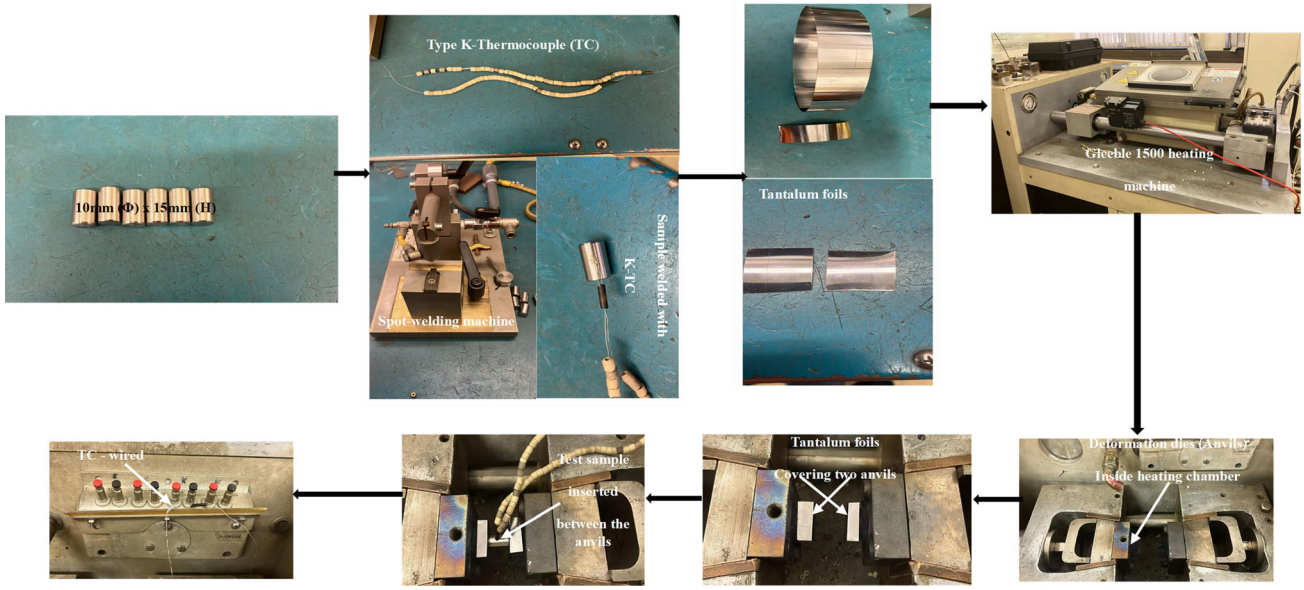

Fig. 7 Schematic representation of sample preparation before hot compression test in a Gleeble 1500

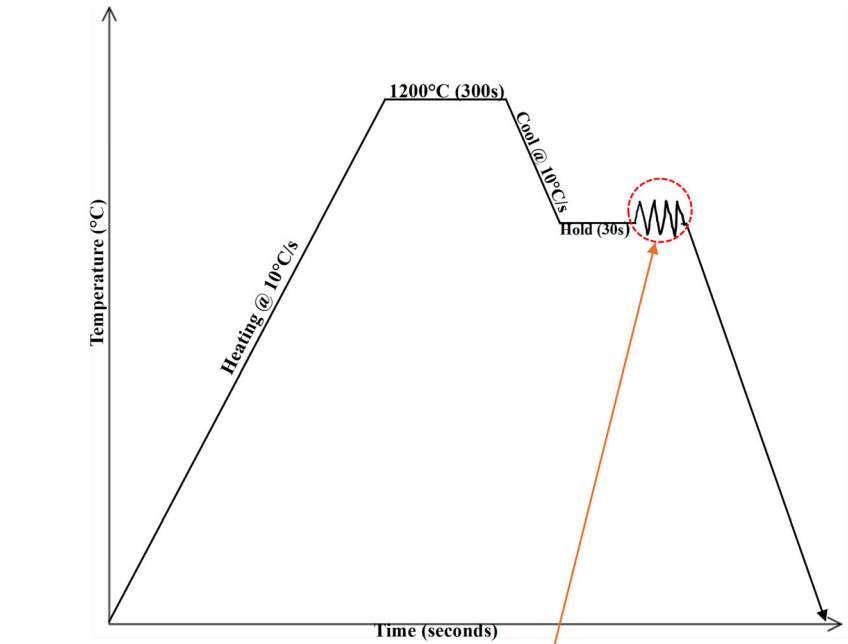

Strain rate (s-1)	850°C	900°C	950°C	1000°C	1050°C
0.001	*S1*	*S6*	*S11*	*S16*	*S21*
0.01	*S2*	*S7*	*S12*	*S17*	*S22*
0.1	*S3*	*S8*	*S13*	*S18*	*S23*
1	*S4*	*S9*	*S14*	*S19*	*S24*
5	*S5*	*S10*	*S15*	*S20*	*S25*

SI = sample ID, I = 1…,25

Fig. 8 Hot deformation cycle used for hot compression tests in a Gleeble 1500D

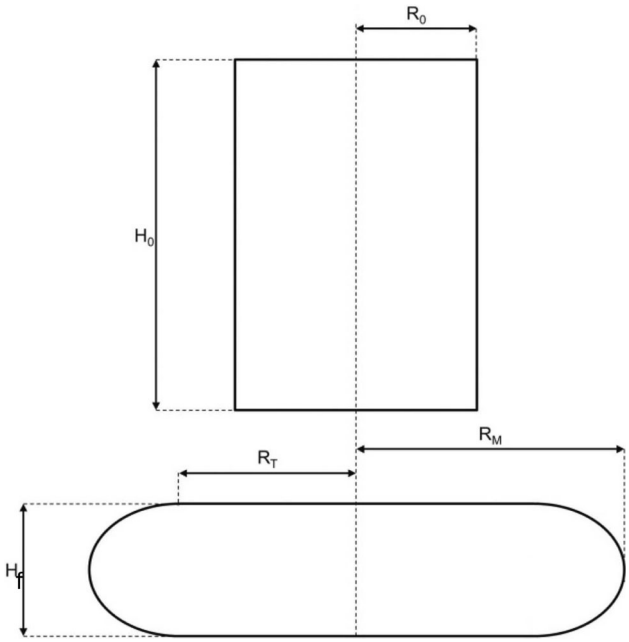

Fig. 9 Illustration diagram showing a cylindrical sample before and after hot compression (Ref 69)

attributed to two folds: (1) sample initially retained heat and increased its temperature causing the Gleeble heating system to decrease heat supply in order to bring sample back to desired temperature, and (2) as deformation progresses the contact area at the interface increases and cause heat loss to the surroundings.

Table 2 Barrelling factor values at various deformation conditions.

Strain rates, s^{-1}	900,°C	950,°C	1000,°C
0.001	1.20	1.15	1.01
0.01	1.29	1.14	1.08
0.1	1.23	1.34	1.08
1	1.24	1.27	1.03
5	1.18	1.17	1.04

Furthermore, a strain rate of 15 s^{-1} was expected to bring a much higher temperature difference than 1 and 5 s^{-1}, however Fig. 11 showed some contradictions. According to Qian et al. (Ref 72), when strain rates are substantial high, the deformation times are much shorter than the response time of the thermocouple. This causes the thermocouple to undergo hysteretic effect, whereby it is incapable of capturing instantaneous temperature changes during the compression test (Ref 73).

Therefore, computation of adiabatic heating by relying on the temperature difference between set and actual temperature from the thermocouple is not advisable when hysteretic behaviour is observed. But rather a theoretical approach as

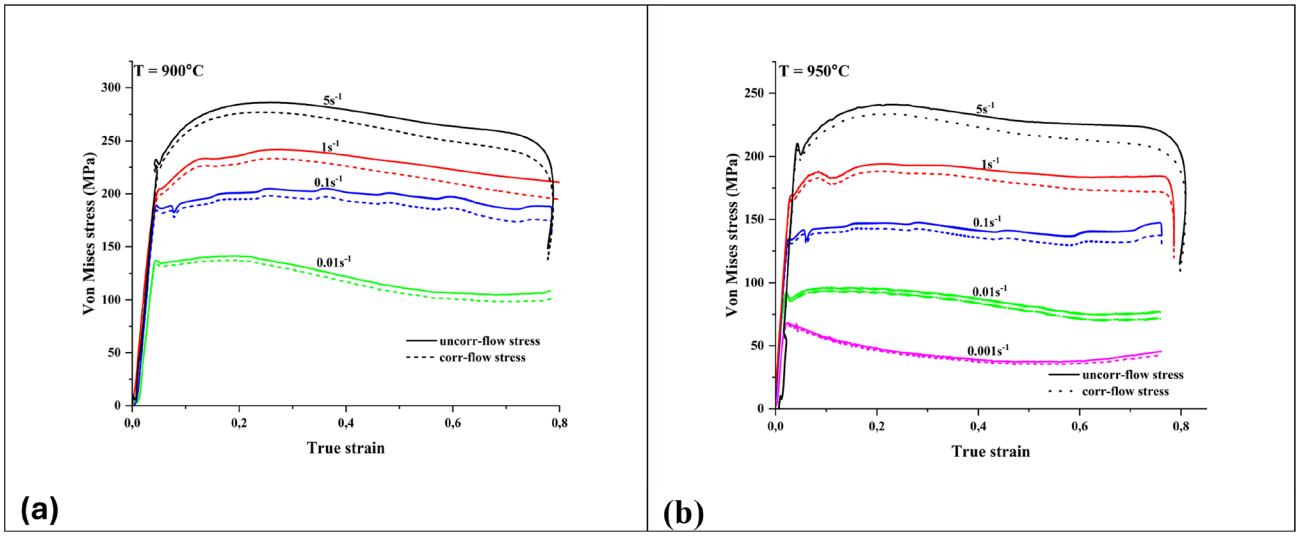

Fig. 10 Non corrected vs corrected flow stress for friction at (a) 900 °C and (b) 950 °C

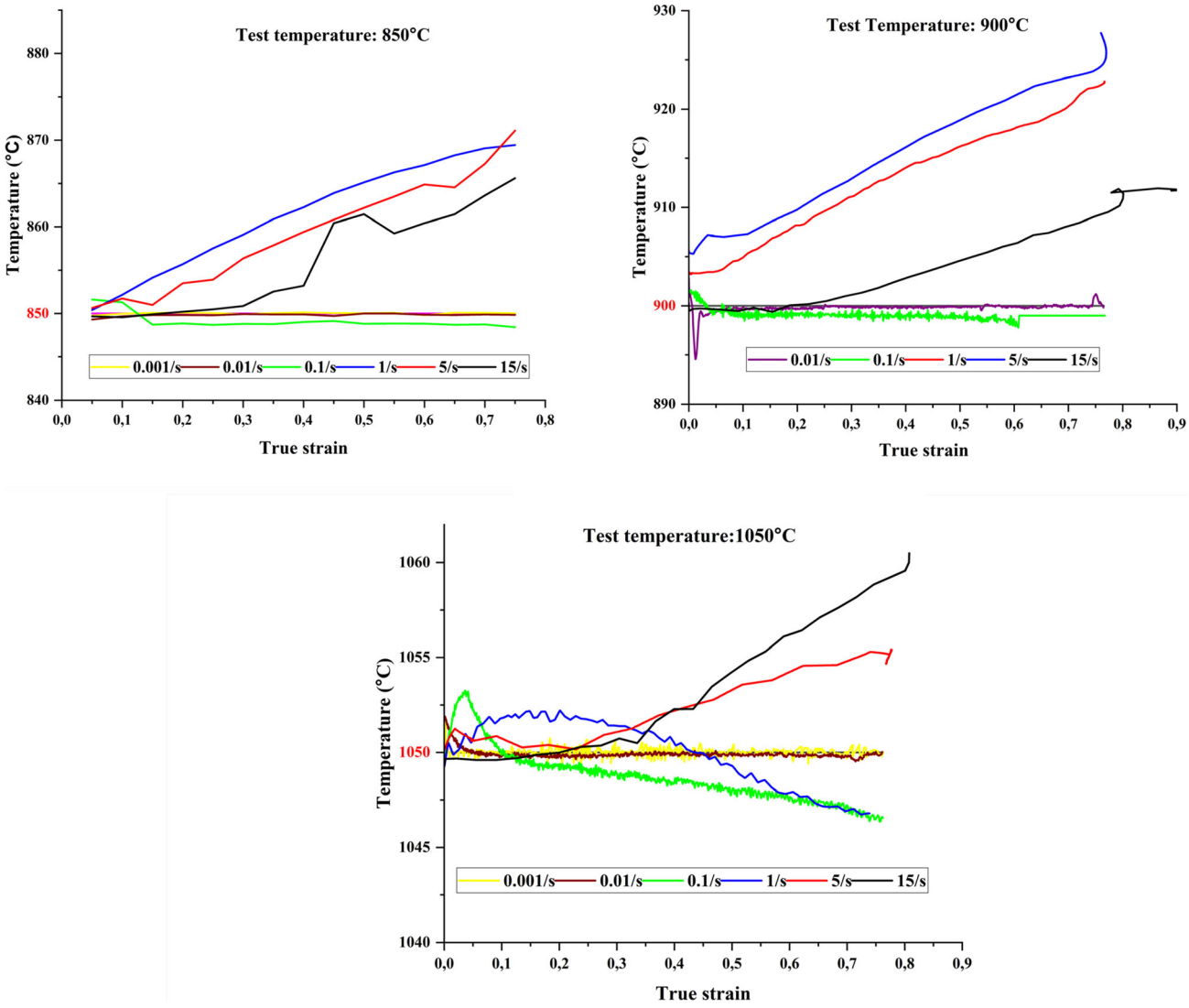

Fig. 11 Set temperature vs actual temperature from k-type thermocouple

suggested by Wang et al., (Ref 73) is recommended when quantifying the change in temperature. This approach involves using (Eq 9) to compute changes in temperature other than taking the difference between set and actual temperature. However, Bodunrin et al., (Ref 66) indicated that theoretical approach may present some errors because (Eq 9) tends to overestimate adiabatic change in temperature. Nevertheless, the theoretical approach has been adopted in many studies of hot deformation (Ref 65, 70, 74, 75) to name a few. Similarly, in this study the temperature changes (ΔT) due adiabatic heating at a strain rate of 1, 5 and 15 s^{-1} were calculated using (Eq 9) below.

$$T = \frac{0.95\eta}{\rho C_p} \int_0^{\varepsilon} \sigma d\varepsilon \quad \text{(Eq 9)}$$

where ρ = density of the 2205 DSS in g/cm^3, C_p = specific heat capacity in J/kgK, η = Taylor Quin coefficient, 0.95 = proportion of stored energy allocated for temperature rise and $\int_0^{\varepsilon} \sigma d\varepsilon$ = area under true-stress strain curve calculated using Origin 2022 software.

The specific heat capacity at various temperatures were calculated using empirical relation found in Kanan et al. (Ref 76) and the results are shown below.

Before adjusting for adiabatic heating, it is important to select a true strain range where correction of flow stress will be based. In this study, a true strain range of {0.05-0.75} was selected. To clarify this, a true strain of 0.05 and strain rate of 1 s^{-1} are selected as an example to show how the flow stress was corrected for localised heating. The followed procedure was adopted from the study conducted by Saxena et al. (Ref 77).

Initially, the ΔT were calculated for each set temperature (T_{set}) using (Eq 9) at mentioned constant strain and strain rate. Followed by addition of ΔT to each T_{set} to get the actual temperatures (T_{actual}). For instance, at 850 °C the actual temperature was calculated as follows and the procedure repeated for all temperatures:

$$T_{actual-850°C} = \Delta T_{850°C} + T_{850°C} \quad \text{(Eq 10)}$$

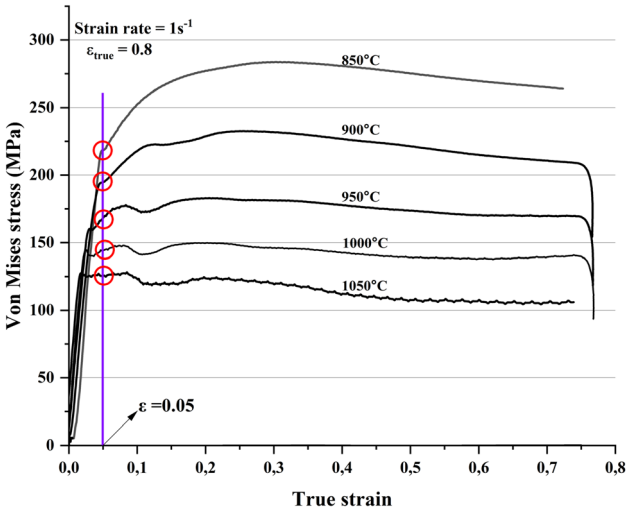

Fig. 12 flow curve @ 1 s^{-1} illustrating extraction of uncorrected flow stress at ε = 0.05

The next step was to find the uncorrected flow stresses (σ_{uncorr}) values (shown within red circles) from the experimental flow curve as demonstrated in Fig. 12 below.

After finding σ_{uncorr} and T_{actual}, the rate at which flow stress was changing per unit increase in temperature was determine by first doing a scatter plot of actual temperature vs uncorrected flow stress. Followed by performing linear regression analysis to find the slope of the linear curve. Where the product of the slope and ΔT was equal to change in flow stress ($\Delta\sigma$) due to adiabatic heating as per following equation:

$$\Delta\sigma = \Delta T * \frac{d\sigma}{dT} \quad \text{(Eq 11)}$$

where $\frac{d\sigma}{dT}$ is the slope from the linear plot of actual temperature vs uncorrected flow stress.

It is worth noting that, the slope from the linear plot must be used to calculate the $\Delta\sigma$ for all temperatures. For instance, at 850 °C the change in flow stress was calculated as follows and the procedure was repeated until 1050 °C

$$\Delta\sigma_{850°C} = \Delta T_{850°C} * \frac{dT}{d\sigma} \quad \text{(Eq 12)}$$

After finding $\Delta\sigma$, it was then added to uncorrected flow stress to get corrected flow stress at each temperature.

$$\sigma_{(corrected)} = \Delta\sigma + \sigma_{uncorrected} \quad \text{(Eq 13)}$$

The above procedure was repeated for each strain until ε = 0.75 at an interval of 0.05 to get all the corrected flow stress. And off course the same procedure was applied for 5 and 15 s^{-1} at the same true strain range. After correction, the corrected flow stresses were plotted against the selected true strain range and then superimposed on the experimental ones as shown in Fig. 13(a) and (b) below for strain rates of 1 and 5 s^{-1} respectively. It can be seen from the flow curves, that low temperatures (850-950 °C) and high strain levels led to considerable softening due to increase in deformation energy. As a result, a large deviation was noticed around these deformation conditions after correction.

The corrected flow curves together with the ones that needed no correction were used to prepare processing maps at various true strains of 0.1, 0.3, 0.5 and 0.8. However, the focus was directed to the PM belonging to 0.8 true strain since the hot compression tests were conducted to a total strain of 0.8.

5. Results and Discussion

5.1 Interpretation of Flow Curves

Figure 14(a) and (b) below shows the flow stress-strain curves of 2205 DSS at constant strain rate and various temperatures. At a glance, it can be easily seen that flow stress of the alloy decreases with rise in temperature for both strain rates. With increase in temperature, thermal barriers to dislocation movement are cancelled out to make the slip process easier, hence a drop in flow stress was observed.

At a strain rate of 5 s^{-1} and across all temperatures, flow stress of an alloy increased till a peak point due to work hardening, then dropped before settling to a steady state. It was noticed that between 950 and 1050 °C, that the drop in flow stress after a peak point was shallow, possible due to sluggish DRX kinetics or DRV coming into play. Further to this,

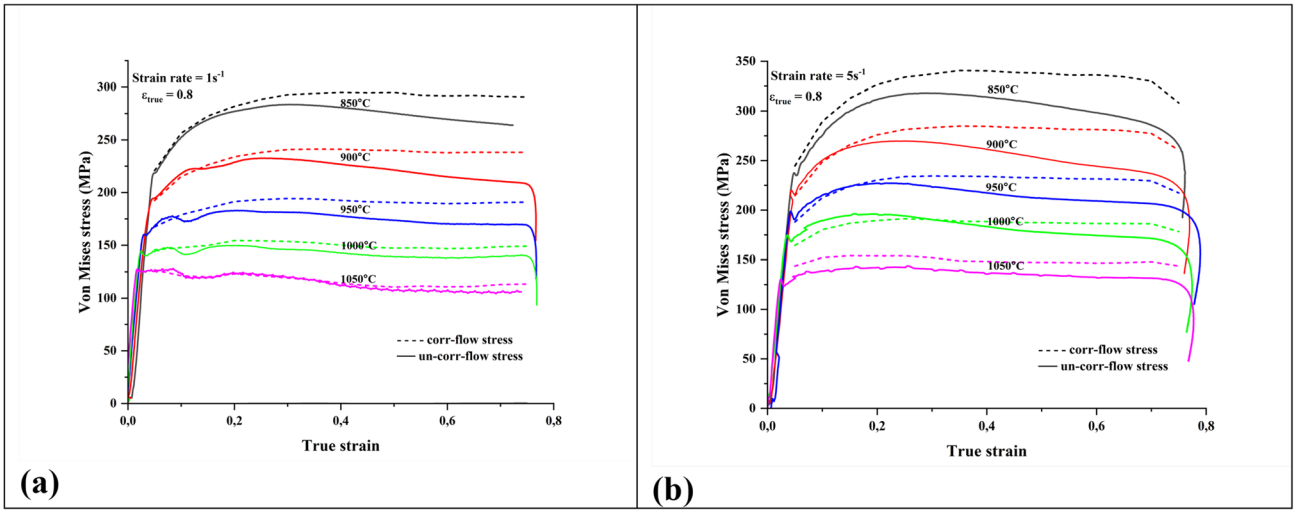

Fig. 13 Flow curves corrected for both friction and adiabatic heating at (a) 1 s^{-1} and (b) 5 s^{-1}

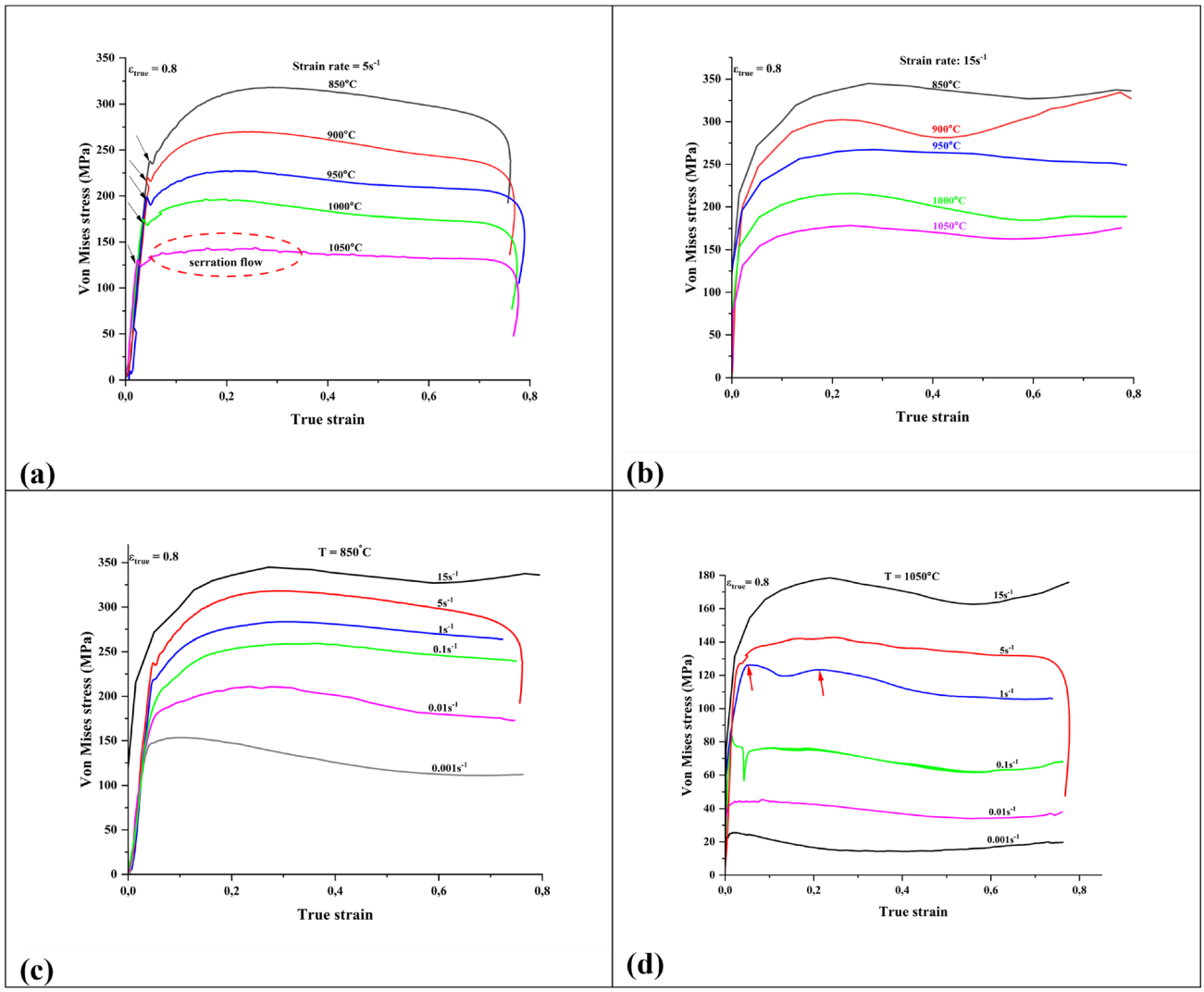

Fig. 14 Flow stress-strain curves of 2205 DSS at various hot processing conditions

temperatures of 850 and 950 °C, showed the absence of steady state due to dominance of softening mechanisms over work hardening. According Chen et al. (Ref 16) absence of steady state region maybe an indication of extensive softening that is associated with flow instabilities other than the DRX process. Another observation at this strain rate was a yield point phenomenon (YPP) after work hardening (indicated by black arrows), which seemed less noticeable with increase in temperature. A possible explanation to YPP could be unlocking of dislocations from interstitial atoms, formation of geometrically necessary dislocations at the grain boundary or strain transfer from ferrite to austenite phase (Ref 24, 25, 78). In addition, diminishing of YPP with increase in temperature could be attributed to increase in diffusional rate of interstitial atoms to an extent that they are able to match the velocity of dislocations and produce homogeneous plastic deformation. Oscillation or multiple peaks before steady state were visible at 1050 °C, this may be ascribed to re-recrystallisation of grains that were recrystallised in the first cycle and the process repeated until steady state is achieved (Ref 79).

Strain rate of 15 s^{-1} and across all temperatures showed flow curves with the characteristics of DRX behaviour. Hot processing at higher strain rates may be accompanied by adiabatic heating, thus softening from the peak stress must be interpreted with caution. This is because formation flow instabilities which manifest themselves in the form of softening, is likely to occur at this magnitude of strain rate. A rise in flow stress at temperatures of 850°, 900 and 1050 °C was noticed at respective true strain, particularly after the steady state was achieved. A similar trend was observed by Zhao et al. (Ref 80) and Wang et al. (Ref 81) who linked post steady state rise in flow stress to increase in friction caused by increase in contact area between the barrelled specimen and the deformation dies or anvils of the thermo-mechanical simulator.

Figure 14(c) and (d) shows the influence of varying the strain rate while holding the temperature constant. Both extreme temperatures showed an increase in flow stress with rise in strain rate. In general, higher strain rate increase the dislocation density and subsequently the formation of dislocation forests or entanglements that act as obstacles to mobile dislocations. In this sense, slip can be restricted and prompt an increase in applied stress for continuous deformation. At lower strain rates (< 1 s^{-1}), flow curves exhibited DRX behavior for both temperatures but 1050 °C showed faster kinetics as indicated by low values of peak strain. At 850 °C /15 s^{-1} a pronounced drop in flow stress was observed but as explained earlier softening at higher strain rate must be interpreted with caution to account for adiabatic heating. Double peaks at 1050 °C/1 s^{-1} (as shown by red arrows) were observed and according to Han et al., (Ref 13) this may be attributed to deformation shift from ferritic to austenitic phase at higher strains. This shift re-initiate work hardening in the latter phase, followed by secondary peak stress before settling to a steady state.

5.2 Interpretation of Processing Maps at 0.1-0.5 True Strain

Figure 15 below shows the PM of 2205 DSS at various true strains that were generated using M-R approach. The contour lines and shaded areas surround safe domains and instability regimes respectively. It can be seen that, areas of low η are associated with instabilities (shaded) areas, whereas unshaded areas had high η indicating absence of instabilities and occurrence of good softening mechanisms. Peak efficiency (η) slightly changed from 41 to 46% at 0.1 and 0.3 true strain respectively and thereafter, maintained at constant value of 43%. Increase in η could be linked to enhancement of deformation kinetics brought by increase in true strain.

At a true strain of 0.1, a peak efficiency of 40% (A) that is likely to be associated with DRX was observed at 1016 °C/0.009 s^{-1}. This was also confirmed from the analysis of flow curves, where a drop in flow stress under similar conditions was observed at a peak strain slightly below 0.1. Two instability regimes associated to low η and negative ξ were also detected at intermediate to high $\dot{\varepsilon}$ range of (0.03 to 0.69) s^{-1}, T = (850-1010) °C and high $\dot{\varepsilon}$ (2.51-15) s^{-1}, T = (956-1022) °C.

At 0.3 true strain, the peak efficiency was still comparable to that one of 0.1 true strain. However, narrowing of instability regimes coupled with addition of a new one at T = (850-925) °C and $\dot{\varepsilon}$ = (2.07-15) s^{-1} was observed at this strain. These results are consistent with Li et al., (Ref 8) who also did PM's of 2205 DSS and observed narrowing of instability regimes with increased in true strain. According to their work (Ref 8), the narrowing was due to improve in ductility of the alloy at certain deformation conditions.

With increase in true strain to 0.5, a safe zone with a peak efficiency of 31% appeared at intermediate temperature (930-970) °C and high strain rate ((4.33-15) s^{-1} ranges. Furthermore, extension of safe working zone to below 900 °C (point B) was observed at low strain rates (0.01-0.08) s^{-1} ranges. A peak efficiency of 43% (point A) was observed at 1008 °C/0.01 s^{-1} deformation conditions. Coalescence of instability area was observed at high T and $\dot{\varepsilon}$, reduction of instability areas at low T and high $\dot{\varepsilon}$.

5.3 Interpretation of 0.8 PM in Conjunction with Microstructural Analysis

Figure 16(a) and (b) below shows PMs prepared using Murty and Rao and Prasad's approach respectively at 0.8 true strain. The preparation and discussion of microstructures were solely based on the former, while the latter is just for comparison. As such, the PM as per Murty and Rao approach was divided into domains and instability regimes and microstructures prepared accordingly.

5.3.1 Safe Domains. Domain #I occurred at a safe hot working zone of low $\dot{\varepsilon}$ range of (0.001-0.06) s^{-1}, low T (850-925) °C and η ranging from 22% to peak of 38.9% at 908 °C/002 s^{-1} (A). Figure 17(a) and (b) shows OM and SEM micrographs respectively that were prepared within this domain at 900 °C/0.01 s^{-1}. The OM micrograph showed islands of elongated austenite grains (white phase) distributed within ferrite matrix (light brown phase) along the rolling direction. Features of DRX from both images included visible substructures (shown by orange arrows) on some of the deformed austenite grains and few recrystallised austenite grains (shown by red circles) on ferrite/ferrite boundaries. These observations suggested that the DRX process could not be completed in austenitic phase, probably due to slow kinetics of grain boundary migration brought in by low temperatures

Both images revealed a relatively high number of high angle boundaries (shown by black arrows) within the ferrite matrix suggesting the mode of softening was more of extended DRV or continuous dynamic recrystallization (CDRX) (Ref 82). The deformation at low strain rates seemed to have supported CDRX into two steps: Firstly, dislocations were given sufficient

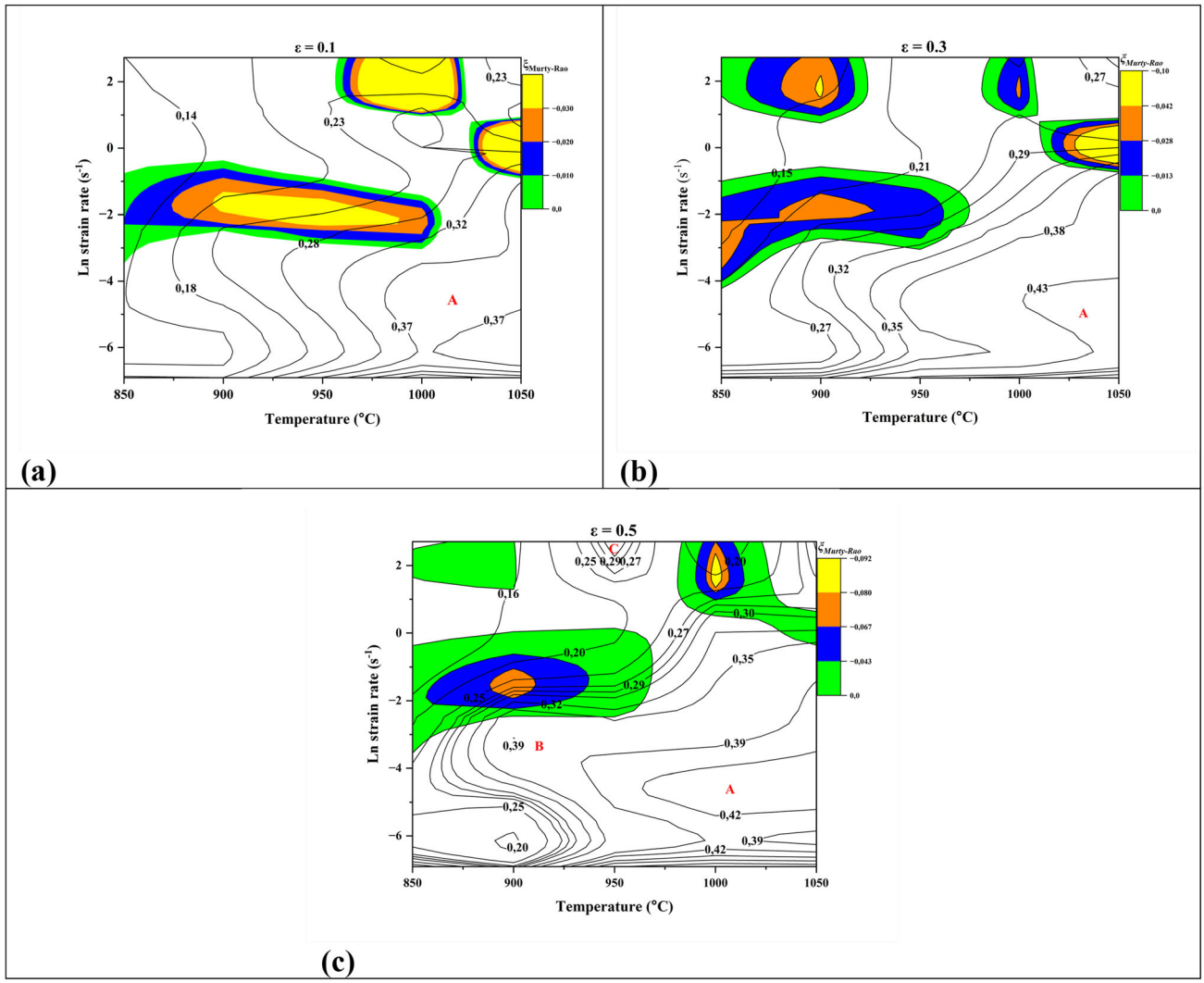

Fig. 15 Processing maps of 2205 DSS at a true strain of: (a) 0.1, (b) 0.3 and (c) 0.5

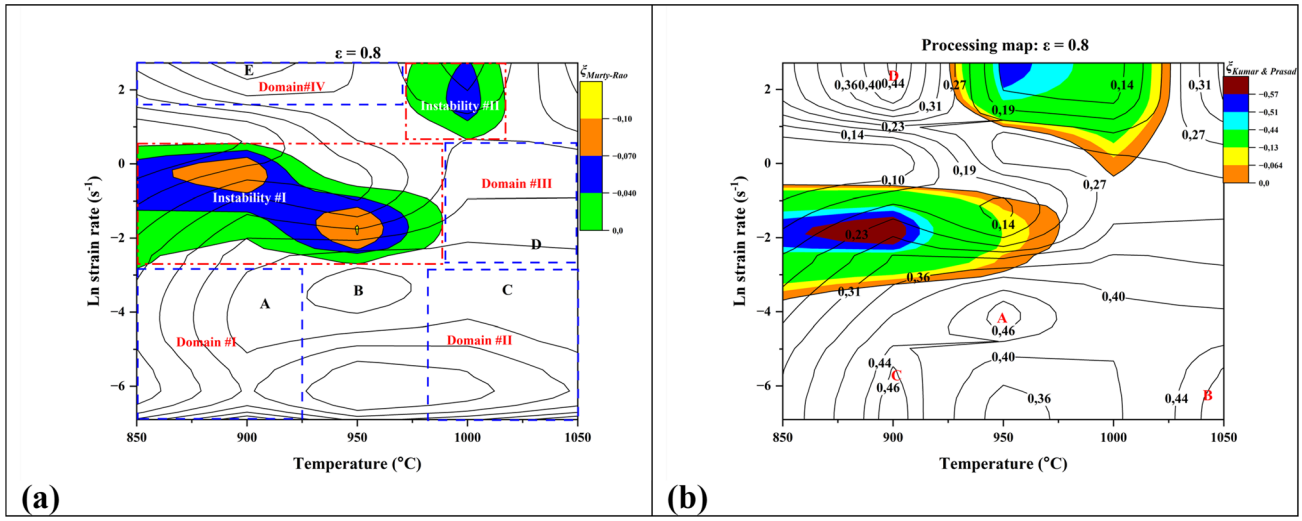

Fig. 16 Processing maps of 2205 DSS: (a) M-R criteria and (b) K-P criteria

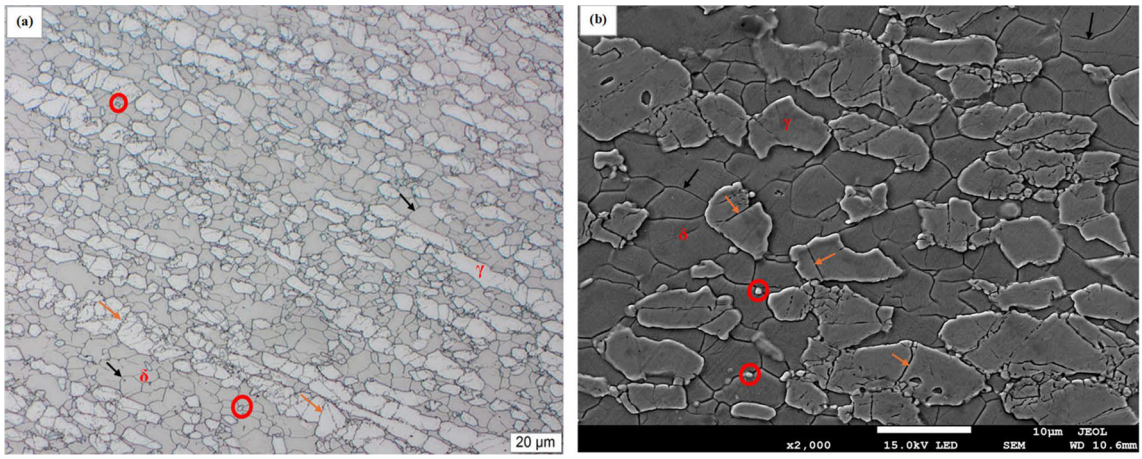

Fig. 17 (a) OM and (b) HRSEM images of 2205 DSS @ 900 °C/0.01 s^{-1}, $\varepsilon = 0.8$

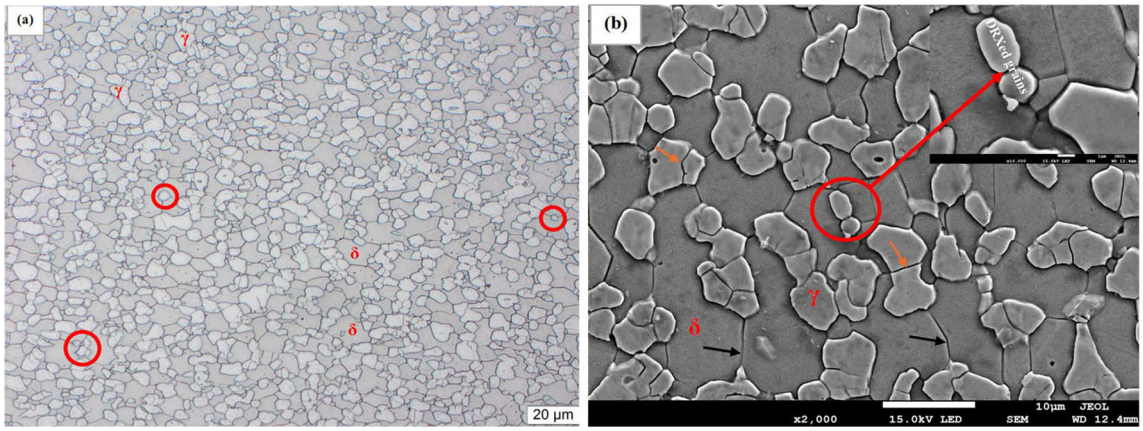

Fig. 18 (a) OM and (b) HRSEM images of 2205 DSS @ 1000 °C/0.01 s^{-1}, $\varepsilon = 0.8$

time to form low angle subgrains within ferrite phase, which is termed DRV, Secondly, with increase in applied strain, these subgrains absorbed dislocations to convert to high angle grain boundaries. The fact that the microstructure obtained within this domain was not uniform, the resulting mechanical properties may not be desirable thus causing this domain not appropriate for hot processing.

Domain #II was a safe domain associated with low $\dot{\varepsilon}$ range of (0.001-0.06) s^{-1}, high T (980-1050) °C and η ranging from 25% to a peak of 38.13% at 1016 °C/003 s^{-1} (C). Efficiencies of domain I, II seemed comparable despite temperature increase. Fig. 18(a) and (b) below shows OM and HRSEM images respectively, prepared within this domain at 1000 °C/0.01 s^{-1}. Both images revealed a fully recrystallised microstructure with equiaxed austenite grains dispersed between ferrite/ferrite high angle grain boundaries. The markings by (red circle) on both images confirmed the DRX process where recrystallised grains of austenite were clearly visible on the ferrite/ferrite boundaries. The observation of equiaxed austenite grains at this low strain rate domain seemed to suggest that the process of DRX was similar to CDRX but occurred via SIBM (Ref 57). In addition, the DRXed grains in this domain were slightly coarser than those observed in domain I, probably due to approximately 100 °C temperature difference or more between the two domains. This increase in temperature may have accelerated the growth of DRXed nuclei through faster grain boundary migration.

DRX was not the only restorative mechanism because visible high angle boundaries (shown by black arrows) on the ferrite matrix confirmed the softening of ferrite by CDRX. The increase in temperature by 100 °C at constant strain rate made the high angle grain boundaries in ferrite to be more visible or rather recognisable in an OM image than those observed in domain I. This could be attributed to more strain being directed to ferrite since austenite volume fraction was diminishing with rise in temperature. Given that this domain produced a homogeneous structure of equiaxed austenite grains randomly distributed within ferrite matrix, the mechanical properties were most likely uniform throughout the structure. Therefore, hot processing of 2205 DSS under this domain was considered ideal even though low strain rate could have a negative impact on the production rate of an industrial hot rolling mill. Despite the use of different approach in designing the processing maps of the current study, the results obtained were comparable to those of Chen et al. (Ref 6), Momeni et al. (Ref 11), Ma et al. (Ref 12), and Li et al., (Ref 8) who used Prasad's approach.

Domain #III occurred at intermediate $\dot{\varepsilon}$ range of (0.07-1.66) s^{-1}, high T (990-1050) °C and η ranging from 29% to a peak of 36.1% at 1030 °C/0.11 s^{-1} (D). Figure 19(a) and (b) below shows OM and HRSEM micrographs that were prepared within this domain at 1000 °C/1 s^{-1}. The alloy seemed to have soften

by both CDRX and DRX. The CDRX features could easily be noticed through well-developed high angle grain boundaries (shown by black arrows) in both images. In an OM image, most deformed austenite grains had deformations twins or bands (shown by red rectangles) which acted as potential nucleation sites for DRXed grains. The increase in strain to 1 s^{-1} at the same temperature as compared to domain II, seemed to have distorted and converted special high angle boundaries (twins) to high angle boundaries probably due to increase in dislocation density. Once twins were distorted, they became highly mobile, serrated, and potential nucleation sites for nucleation of austenite grains as shown in red rectangles from SEM image. This observation confirmed that with increase in strain rate, DRX of austenite occurs via distortion of special high angle grain boundaries than SIBM. Even though both softening mechanisms were operative, the microstructure showed a mixture of recrystallised and un-recrystallised austenite grains, probably due to low kinetics of DRX at these deformation conditions. Therefore, non-uniform mechanical properties may be realised from this typical structure.

Domain #IV occurred at high $\dot{\varepsilon}$ range of (5.04-15.1) s^{-1}, low to intermediate T (850-970) °C and η ranging from 22% to a peak of 34.6% at 900 °C/13.5 s^{-1} (E). Figure 20(a) and (b) below shows OM and HRSEM micrographs which were prepared within this domain at 900 °C/15 s^{-1}. Referring back to the flow curves in Fig. 14(b) a significant drop in flow stress after reaching peak is thought to have occurred due to DRX at play. Therefore, it was expected that these conditions should have refined the austenitic phase, given that its low SFE and present in greater proportion at 900 °C. However, the microstructure prepared within this domain proved otherwise, ferrite matrix was substantially refined while the austenite grains remained deformed along the working direction with sub-boundaries and deformation bands (hand circled in yellow). This then suggested that the observed drop in flow stress at 900 °C/15 s^{-1} could have been localised heating of the sample brought by high strain rate and low temperature. The substantial grain refinement of ferrite grains is thought to have occurred by means of discontinuous dynamic recrystallisation (DDRX). This was confirmed through SEM image that revealed a large distribution of equiaxed ferrite grains (circled in white) throughout the ferrite matrix. The OM image also revealed equiaxed ferrite grains bounded by high angle grain boundaries (marked in black), and partly covered by deformed austenite grains (white phase) with substructures (marked in yellow). Even though deformed austenite grains showed quite a large number of substructures as per both images, very few showed some evidence of nucleation taking place. The SEM image confirmed a small fraction of nucleation of austenite grains from the substructures (see yellow marking). The occurrence of DDRX in ferritic phase is very rare, but have been reported by Haghdadi et al., (Ref 60) at high strain rates, where less time is

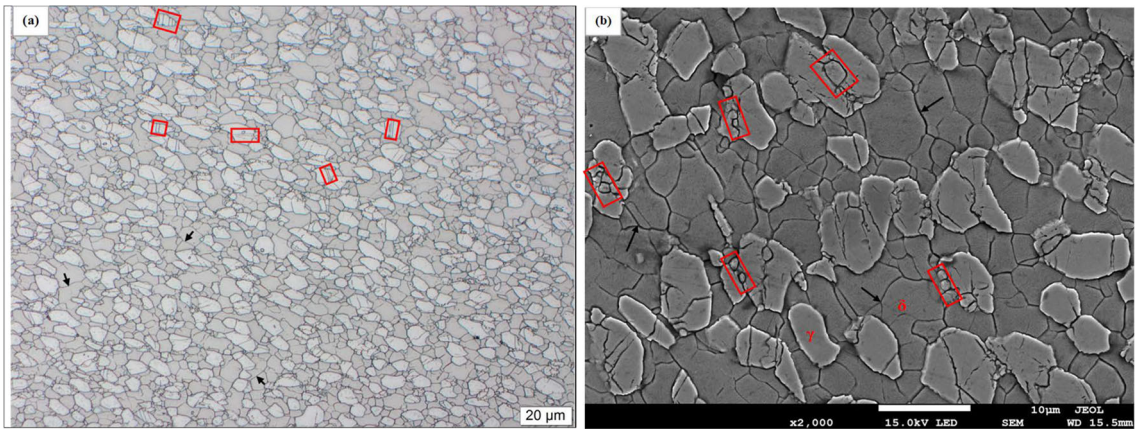

Fig. 19 (a) OM and (b) HRSEM images of 2205 DSS @ 1000 °C/1 s^{-1}, $\varepsilon = 0.8$

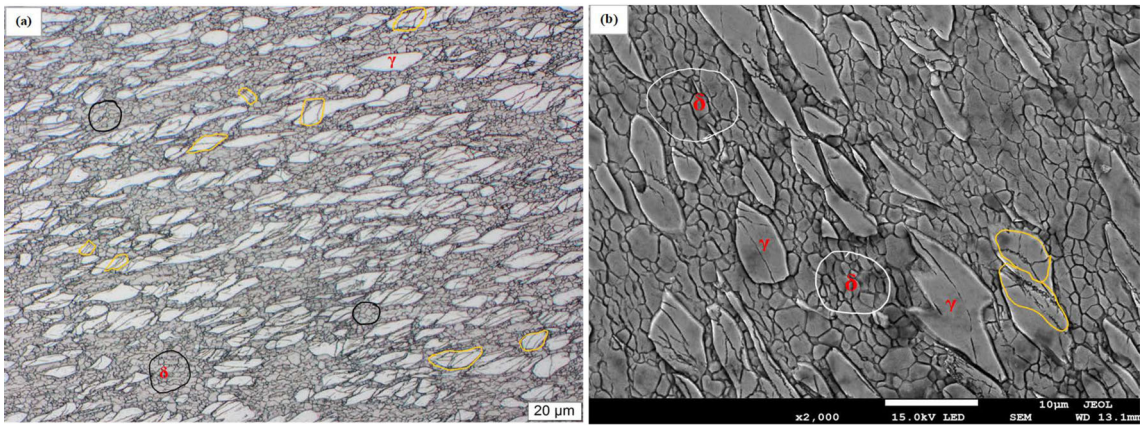

Fig. 20 (a) OM and (b) HRSEM images of 2205 DSS @ @ 900 °C/15 s^{-1}, $\varepsilon = 0.8$

Table 3 Thermo-physical properties of 2205 DSS

Thermo-physical property	850,°C	900,°C	950,°C	1000,°C	1050,°C
ρ, g cm^{-3}	7.860				
C_p, J kgK^{-1}	587.23	594.32	602.31	611.30	621.40

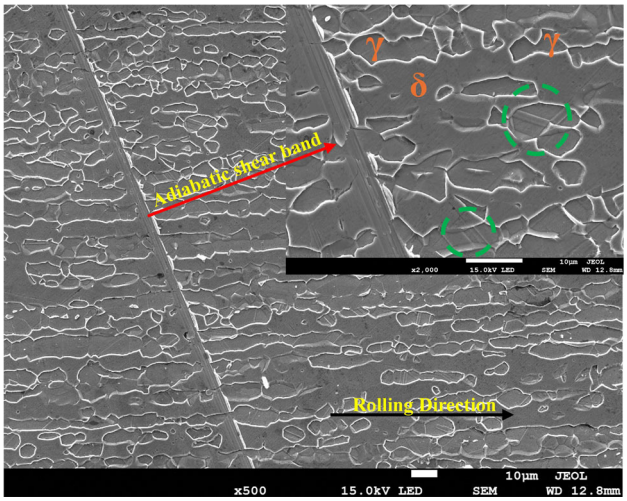

Fig. 21 HRSEM image of 2205 DSS at 1000 °C/15 s^{-1}

available for subgrains to form and induce CDRX. The microstructure from this domain showed that ferrite matrix was refined by means of DDRX, and most of deformed austenite grains had substructures but not fully recrystallized. This typical non-homogeneous microstructure could have an impact on the uniformity of mechanical properties. Therefore, processing at this window can only be recommended if hot processing parameters are carefully controlled to avoid partial DRX.

5.3.2 Instability Regimes. Instability regimes are regarded as unsafe zones and pose a potential risks of flow instabilities. Any hot processing done at these zones affect structural integrity of the rolled product. In this work, it was observed that these regimes vary with true strain, in a sense that they narrowed in terms of area or appeared in small numbers at deformation progress. A possible explanation was found in Li et al., (Ref 8) who attributed narrowing of regimes to improve in ductility of the alloy. A similar trend was observed in this work where instability regimes reduced from 4 ($\varepsilon = 0.3$) to 2 ($\varepsilon = 0.8$). The root cause of one-instability regime (II) occurred at $\varepsilon = 0.8$ is explained below (Table 3).

5.3.2.1 Instability Regime II. This regime occurred at higher strain rate range of (1.95-15) s^{-1}, intermediate to high T (972-1017) °C and $\xi < 0$. HRSEM micrograph was prepared within this regime at 1000 °C/15 s^{-1} to check for occurrence of flow instabilities. Adiabatic shear band (ASB) oriented almost 45° with respect to compression axis and mechanical twins (circled in green) were identified as shown in Fig. 21 below. Formation of ASB was believed to be the consequences of localised heating brought by hot processing at higher strain rate and low to moderate temperatures. Under these deformation conditions heat extraction from certain region of the microstructure was not sufficient, resulting in a localised drop in flow stress and severe plastic deformation. Furthermore, higher strain rates brought additional flow stress that may have caused the widening of stacking fault regions in austenitic phase. This obviously could have lowered the SFE of the phase to make the formation of mechanical twins easier (Ref 83).

5.3.3 Application of PM to Industrial Hot Rolling Mills. In general, low strain rates range showed a good efficiency when compared to intermediate or higher strain rate ranges. However, any processing done at low strain rate may hamper the production rate of the industrial hot mills. Furthermore, processing at higher temperatures gives the benefit of lower rolling forces, but the energy consumption of the hot mill may skyrocket the electricity costs and of which this is unbeneficial from the economic point of view. Industrial hot rolling operations are normally operated at higher strain rates that could range from 1 s^{-1} to as high as 100 s^{-1} (Ref 55). In this work, a possible hot working window located at higher strain rates (5.04-15) s^{-1} and low to intermediate temperature (850-970) °C was identified. Even though this window was coupled with a 34.6% moderate efficiency, it was considered as an option on the basis of faster production rate when compared to lower strain rate region. However, strict control of deformation parameters is crucial to optimise DRX kinetics and elimination the potential risk of flow instabilities (Ref 47).

6. Conclusions

Stable und unstable zones during hot processing of 2205 DSS were investigated using modified dynamic material modeling (MDMM) suggested by Murty and Rao. The following conclusions were drawn from the study.

- Hot processing of 2205 DSS at higher strain rates and intermediate to high temperature leads to instability regimes that are associated with formation of mechanical twins and adiabatic shear bands. These regimes seemed to prevail at lower strain region and reduced as the strain increases.
- At lower strain rates and across all temperatures, the energy dissipated was well utilised by good restoration mechanisms as indicated by high dissipation efficiency (>40%) and defect-free microstructure.
- Low strain rates seemed to be a good hot working window for hot processing. However, hot industrial rolling mills should make trade-offs between high production rate and good quality rolled products.
- Higher strain rates (>5 s^{-1}) and low temperature (<972 °C) also presented a moderate efficiency (≈35%) with inhomogeneous microstructure and presumably non-uniform mechanical properties.

- Hot processing of 2205 DSS at higher strain rates and low temperature is recommended if deformation parameters are strictly controlled to optimise the kinetics of restorative mechanisms, particularly DRX.
- The obtained results from this study showed not much difference between Murty's and Prasad's approach in terms of identification of instabilities. However, the former approach seemed to predict narrow range of instability regimes.

Acknowledgments

The authors would like to thank the following institutions and research centres who made this research paper possible: DHET University Capacity Development Grant (UCDP) at University of Johannesburg for funding the project. Industrial Minerals and Metals Research Institute (IMMRI) at University of Pretoria (UP) for providing access to Gleeble thermo-mechanical simulator. Center for Nanoengineering and Advanced Materials (CeNAM) for giving access to their high-resolution scanning electron microscope (HRSEM).

Funding

Open access funding provided by University of Johannesburg.

Open Access

References

1. Y. Han, D. Zou, Z. Chen, G. Fan, and W. Zhang, Investigation on Hot Deformation Behavior of 00Cr23Ni4N Duplex Stainless Steel Under Medium-High Strain Rates, *Mater Charact*, 2011, **62**(2), p 198–203. https://doi.org/10.1016/j.matchar.2010.11.013
2. M. Faccoli and R. Roberti, Study of Hot Deformation Behaviour of 2205 Duplex Stainless Steel Through Hot Tension Tests, *J. Mater. Sci.*, 2013, **48**(15), p 5196–5203. https://doi.org/10.1007/s10853-013-7307-8
3. J. Moon, H.H. Jo, H.Y. Ha, S.D. Kim, T.H. Lee, and C.H. Lee, Microstructure Evolution and Hot Deformation Behavior of 25Cr–6Mn–3Ni–1Mo–3W–0.1C–0.34N Lean Duplex Stainless Steel, *J. Mater. Res. Technol.*, 2021, **14**, p 186–194. https://doi.org/10.1016/j.jmrt.2021.06.075
4. G. E. Dieter, H. a. Kuhn, and S. L. Semiatin, *Handbook of Workability and Process Design*. 2003
5. S.V.S. Narayana Murty, B. Nageswara Rao, and B.P. Kashyap, Instability criteria for hot deformation of materials, *Int. Mater. Rev.*, 2000, **45**(1), p 15–26. https://doi.org/10.1179/095066000771048782
6. L. Chen, X. Ma, X. Liu, and L. Wang, Processing Map for Hot Working Characteristics of a Wrought 2205 Duplex Stainless Steel, *Mater. Des.*, 2011, **32**(3), p 1292–1297. https://doi.org/10.1016/j.matdes.2010.09.030
7. W. Min et al., Hot Deformation Behavior and Softening Mechanism of As-Cast S32750 Super Duplex Stainless Steel at Low and High Strain Rates, *J. Mater. Eng. Perform.*, 2020, **29**(2), p 727–738. https://doi.org/10.1007/s11665-020-04571-w
8. Q. Li et al., Strain Rate and Temperature Sensitivity on the Flow Behaviour of a Duplex Stainless Steel During Hot Deformation, *Mater. Technol.*, 2023, **38**(1), p 1–10. https://doi.org/10.1080/10667857.2023.2166216
9. Y. Zhao, Y. Wang, S. Tang, W. Zhang, and Z. Liu, Development of a Novel Cr21 Lean Duplex Stainless Steel and Its Hot Deformation Behavior, *J. Mater. Eng. Perform.*, 2019, **28**(1), p 296–307. https://doi.org/10.1007/s11665-018-3830-8
10. Y.V.R.K. Prasad, Processing Maps: A Status Report, *J. Mater. Eng. Perform.*, 2013, **22**(10), p 2867–2874. https://doi.org/10.1007/s11665-013-0732-7
11. A. Momeni, K. Dehghani, G.R. Ebrahimi, and S. Kazemi, Developing the Processing Maps Using the Hyperbolic Sine Constitutive Equation, *Metall. Mater. Trans. A Phys. Metall. Mater. Sci.*, 2013, **44**(12), p 5567–5576
12. M. Ma, H. Ding, Z. Tang, J. Zhao, Z. Jiang, and G. Li, Effect of Strain Rate and Temperature on Hot Workability and Flow Behaviour of Duplex Stainless Steel, *Ironmak. Steelmak.*, 2016, **43**(2), p 88–96. https://doi.org/10.1179/1743281215Y.0000000053
13. J. Han, J.P. Sun, Y. Han, and H. Liu, Hot Workability of the As-Cast 21Cr Economical Duplex Stainless Steel Through Processing Map and Microstructural Studies Using Different Instability Criteria, *Acta Metall. Sin.*, 2017, **30**(11), p 1080–1088. https://doi.org/10.1007/s40195-017-0647-7
14. J.L. Zhang, H.Z. Guo, and H.Q. Liang, Hot Deformation Behavior and Process Parameter Optimization of Ti22Al25Nb Using Processing Map, *Rare Met.*, 2016, **35**(1), p 118–126. https://doi.org/10.1007/s12598-015-0646-7
15. Y. Zhang, Q. Fan, X. Zhang, Z. Zhou, Z. Xia, and Z. Qian, Avrami Kinetic-Based Constitutive Relationship for Armco-Type Pure Iron in Hot Deformation, *Metals*, 2019 https://doi.org/10.3390/met9030365
16. L. Chen, X. Ma, X. Liu, and L. Wang, Processing Map for Hot Working Characteristics of a Wrought 2205 Duplex Stainless Steel, *Mater. Des.*, 2011 https://doi.org/10.1016/j.matdes.2010.09.030
17. M.S. Ghazani and B. Eghbali, Prediction of Post-deformation Recrystallization Kinetics in AISI 321 Austenitic Stainless Steel Using Double-Stage Hot Compression, *J. Mater. Eng. Perform.*, 2024, **28**(6), p 3563–3571. https://doi.org/10.1007/s11665-019-04139-3
18. A. Sarkar et al., Kinetics of Dynamic Recrystallization in Cobalt: A Study Using the Avrami Relation, *Phys. Status Solidi (a)*, 2011, **818**(4), p 814–818. https://doi.org/10.1002/pssa.201127001
19. S.H. Zahiri, C.H.J. Davies, and P.D. Hodgson, A Mechanical Approach to Quantify Dynamic Recrystallization in Polycrystalline Metals, *Scr. Mater.*, 2005, **52**(4), p 299–304. https://doi.org/10.1016/j.scriptamat.2004.10.011
20. H. Mirzadeh, J.M. Cabrera, J.M. Prado, and A. Najafizadeh, Hot Deformation Behavior of a Medium Carbon Microalloyed Steel, *Mater. Sci. Eng. A*, 2011, **528**(10–11), p 3876–3882. https://doi.org/10.1016/j.msea.2011.01.098
21. S. M. Abbasi, A. Momeni, M. Morakkabati, and R. Mahdavi, Influence of Hot Working on Mechanical and Physical Properties of an Fe – Ni – Co alloy, pp. 1–9
22. Y.J. Zhang, G.L. Wu, and S.W. Wu, The Critical Conditions and Kinetics Required for Dynamic Recrystallization in a High-Carbon Tool Steel, *Arch. Metall. Mater.*, 2021, **66**(1), p 119–125. https://doi.org/10.24425/amm.2021.134767
23. C. Li, L. Huang, M. Zhao, X. Zhang, J. Li, and P. Li, Influence of Hot Deformation On Dynamic Recrystallization Behavior of 300M Steel: Rules and Modeling, *Mater. Sci. Eng. A*, 2020, **797**, p 139925. https://doi.org/10.1016/j.msea.2020.139925
24. H.Z. Zhao, L. Xiao, P. Ge, J. Sun, and Z.P. Xi, Hot Deformation Behavior and Processing Maps of Ti-1300 Alloy, *Mater. Sci. Eng. A*, 2014, **604**, p 111–116. https://doi.org/10.1016/j.msea.2014.03.016

25. Y.H. Mozumder, K. Arun Babu, R. Saha, and S. Mandal, Flow Characteristics and Hot Workability Studies of a Ni-Containing Fe-Mn-Al-C Lightweight Duplex Steel, *Mater Charact*, 2018, **146**, p 1–14. https://doi.org/10.1016/j.matchar.2018.09.036
26. Y. V. R. K. Prasad, K. P. Rao, and S. Sasidhara, *Hot Working Guide*. 2015. [Online]. Available: http://linkinghub.elsevier.com/retrieve/pii/B978080033454750019X
27. Y.V.R.K. Prasad and T. Seshacharyulu, Modelling of Hot Deformation for Microstructural Control, *Int. Mater. Rev.*, 1998, **43**(6), p 243–258. https://doi.org/10.1179/imr.1998.43.6.243
28. Y. Han, G. Liu, D. Zou, R. Liu, and G. Qiao, Deformation Behavior and Microstructural Evolution of As-Cast 904L Austenitic Stainless Steel During Hot Compression, *Mater. Sci. Eng. A*, 2013, **565**, p 342–350. https://doi.org/10.1016/j.msea.2012.12.043
29. Z. Du, S. Jiang, and K. Zhang, The Hot Deformation Behavior and Processing Map of Ti-47.5Al-Cr-V Alloy, *Mater. Des.*, 2015, **86**, p 464–473. https://doi.org/10.1016/j.matdes.2015.07.027
30. B. Gong, X.W. Duan, J.S. Liu, and J.J. Liu, A Physically Based Constitutive Model of As-Forged 34CrNiMo6 Steel and Processing Maps for Hot Working, *Vacuum*, 2018, **155**, p 345–357. https://doi.org/10.1016/j.vacuum.2018.06.022
31. J.K. Fan, H.C. Kou, M.J. Lai, B. Tang, H. Chang, and J.S. Li, Characterization of Hot Deformation Behavior of a New Near Beta Titanium Alloy: Ti-7333, *Mater. Des.*, 2013, **49**, p 945–952. https://doi.org/10.1016/j.matdes.2013.02.044
32. Y.L. Fang, Z.Y. Liu, H.M. Song, and L.Z. Jiang, Hot Deformation Behavior of a New Austenite-Ferrite Duplex Stainless Steel Containing High Content of Nitrogen, *Mater. Sci. Eng. A*, 2009, **526**(1–2), p 128–133. https://doi.org/10.1016/j.msea.2009.07.012
33. G. E. Dieter and D. Bacon, *Mechanical Metallurgy MECHANICAL Adapted by*. 1988
34. J. Lu, Y. Song, L. Hua, K. Zheng, and D. Dai, Thermal Deformation Behavior and Processing Maps of 7075 Aluminum Alloy Sheet Based on Isothermal Uniaxial Tensile Tests, *J. Alloys Compd.*, 2018, **767**, p 856–869. https://doi.org/10.1016/j.jallcom.2018.07.173
35. Y. Tong, G. Zheng Quan, J. Zhao, Q. Liu, W. Xiong, and R. Ju Shi, Double Identification of the Optimal Hot Deformation Parameter Windows for AlCu4SiMg Alloy, *Mater. Res.*, 2019, **22**(4), p e20190131. https://doi.org/10.1590/1980-5373-MR-2019-0131
36. H. Ahamed and V. Senthilkumar, Hot Deformation Behavior of Mechanically Alloyed Al6063/0.75Al_2O_3/0.75Y_2O_3 Nano-Composite: A Study Using Constitutive Modeling and Processing Map, *Mater. Sci. Eng. A*, 2012, **539**, p 349–359. https://doi.org/10.1016/j.msea.2012.01.109
37. C. Zhang, L. Zhang, W. Shen, M. Li, and S. Gu, Characterization of Hot Deformation Behavior of Hastelloy C-276 Using Constitutive Equation and Processing Map, *J. Mater. Eng. Perform.*, 2015, **24**(1), p 149–157. https://doi.org/10.1007/s11665-014-1310-3
38. N. Nayan, G. Singh, S.V.S. Narayana Murty, A.K. Jha, B. Pant, and K.M. George, High-Temperature Deformation Processing Map Approach for Obtaining the Desired Microstructure in a Multi-component (Ni-Ti-Cu-Fe) Alloy, *Metall. Mater. Trans. A Phys. Metall. Mater. Sci.*, 2015, **46**(5), p 2201–2215. https://doi.org/10.1007/s11661-015-2799-2
39. Y. Han, Y. Sun, W. Zhang, and H. Chen, Hot Deformation and Processing Window Optimization of a 70MnSiCrMo Carbide-Free Bainitic Steel, *Materials*, 2017, **10**(3), p 318. https://doi.org/10.3390/ma10030318
40. O. Deformation, "One-Pass Deformation," 2021
41. W. Feng, F. Qin, and H. Long, Hot Workability Analysis and Processing Parameters Optimisation for 20CrMnTiH Steel by Combining Processing Map with Microstructure, *Ironmak. Steelmak.*, 2018, **45**(4), p 317–324. https://doi.org/10.1080/03019233.2016.1264145
42. G. Zheng Quan, Y. Wang, C. Tang Yu, and J. Zhou, Hot Workability Characteristics of As-Cast Titanium Alloy Ti-6Al-2Zr-1Mo-1V: A Study Using Processing Map, *Mater. Sci. Eng. A*, 2013, **564**, p 46–56
43. Y. Li, H. Ji, W. Li, Y. Li, W. Pei, and J. Liu, Hot Deformation Characteristics-Constitutive Equation and Processing Maps-of 21–4N Heat- Resistant Steel, *Materials*, 2018, **12**(1), p 89. https://doi.org/10.3390/ma12010089
44. X. Wang, Z. Liu, and H. Luo, Hot Deformation Characterization of Ultrahigh Strength Stainless Steel Through Processing Maps Generated Using Different Instability Criteria, *Mater Charact*, 2017, **131**, p 480–491. https://doi.org/10.1016/j.matchar.2017.07.041
45. N. Neethu and P. Chakravarthy, Development of Processing Maps for Hot Deformation: Algorithm and Common Errors, *Metall. Mater. Trans. A Phys. Metall. Mater. Sci.*, 2020, **51**(7), p 3398–3402. https://doi.org/10.1007/s11661-020-05817-x
46. S.V.S. Narayana Murty and B. Nageswara Rao, On the Flow Localization Concepts in the Processing Maps of Titanium Alloy Ti-24Al-20Nb, *J. Mater. Process. Technol.*, 2000, **104**(1), p 103–109. https://doi.org/10.1016/S0924-0136(00)00517-3
47. H. Zhao et al., Hot Deformation Behaviour of 40CrNi Steel and Evaluation of Different Processing Map Construction Methods, *J. Mater. Res. Technol.*, 2020, **9**(3), p 2856–2869. https://doi.org/10.1016/j.jmrt.2020.01.020
48. D. Huang and W. Feng, Hot Deformation Characteristics and Processing Map of FV520B Martensitic Precipitation-Hardened Stainless Steel, *J. Mater. Eng. Perform.*, 2019, **28**(4), p 2281–2291. https://doi.org/10.1007/s11665-019-03974-8
49. A. Al Omar and J.M. Prado, Criteria for Prediction of Plastic Instabilities for Hot Working Processes (Part I: Theoretical Review), *Weld. Int.*, 2012, **26**(12), p 921–934. https://doi.org/10.1080/09507116.2011.592704
50. J. Zhang, H. Di, H. Wang, K. Mao, T. Ma, and Y. Cao, Hot Deformation Behavior of Ti-15-3 Titanium Alloy: A Study Using Processing Maps, Activation Energy Map, and Zener-Hollomon Parameter Map, *J. Mater. Sci.*, 2012, **47**(9), p 4000–4011. https://doi.org/10.1007/s10853-012-6253-1
51. H.T. Jeong, H.K. Kim, and W.J. Kim, Processing Maps (With Flow Instability Criterion Based on Power-Law Breakdown) Integrated Into Finite Element Simulations for Evaluating the Hot Workability of 7075 Aluminum Alloy, *Mater. Today Commun.*, 2021, **27**, p 102254. https://doi.org/10.1016/j.mtcomm.2021.102254
52. Q. Li, H. Bu, J. Han, and M. Li, Dynamic Recrystallization Behavior and Processing Maps of 5CrNiMoV Steel During Hot Deformation, *Mater. Res. Express*, 2023, **10**(4), p 046519. https://doi.org/10.1088/2053-1591/acce22
53. K. Huang and R.E. Logé, A Review of Dynamic Recrystallization Phenomena in Metallic Materials, *Mater. Des.*, 2016, **111**, p 548–574. https://doi.org/10.1016/j.matdes.2016.09.012
54. J. Dong, K. Li, Z. Shao, L. Peng, and C. Li, Dynamic Recrystallization Behavior and Mechanism of Fe–Cr–Ni–Mn–Mo–N Low Magnetic Stainless Steel During Hot Deformation, *J. Mater. Sci.*, 2023, **58**(40), p 15845–15860. https://doi.org/10.1007/s10853-023-08916-3
55. F. J. Humphreys, M. Matherly, 6.1.1 The occurrence of recovery. *Recryst. Relat. Annelaling Phenom.*, pp. 437–444, 2004
56. W. Chen, C. Zheng, and L. Dianzhong, The Operative Dynamic Recrystallization Mechanism of Austenite During the Transient Deformation in a Ni-30%Fe Model Alloy, *J. Phys. Conf. Ser.*, 2019, **1270**(1), p 1–6. https://doi.org/10.1088/1742-6596/1270/1/012047
57. W. Chen, C. Zheng, C. Jia, B. Hu, and D. Li, Strain-Rate Dependence of the Dynamic Softening in a Duplex Stainless Steel, *Mater Charact*, 2020, **162**, p 110219. https://doi.org/10.1016/j.matchar.2020.110219
58. N. Haghdadi, P. Cizek, H. Beladi, and P.D. Hodgson, Dynamic Restoration Processes in a 23Cr-6Ni-3Mo Duplex Stainless Steel: Effect of Austenite Morphology and Interface Characteristics, *Metall. Mater. Trans. A Phys. Metall. Mater. Sci.*, 2017, **48**(10), p 4803–4820. https://doi.org/10.1007/s11661-017-4227-2
59. N. Haghdadi, P. Cizek, H. Beladi, and P.D. Hodgson, The Austenite Microstructure Evolution in a Duplex Stainless Steel Subjected to Hot Deformation, *Philos. Mag.*, 2017, **97**(15), p 1209–1237. https://doi.org/10.1080/14786435.2017.1293860
60. N. Haghdadi, P. Cizek, H. Beladi, and P.D. Hodgson, Hot Deformation and Restoration Mechanisms in Duplex Stainless Steels: Effect of Strain Rate, *Metall. Ital.*, 2017, **109**(9), p 5–16
61. X. Gao, H. Bin Wu, M. Liu, Y. Xiang Zhang, and X. Dong Zhou, Dynamic Recovery and Recrystallization Behaviors of C71500 Copper-Nickel Alloy Under Hot Deformation, *J. Mater. Eng. Perform.*, 2020, **29**(11), p 7678–7692. https://doi.org/10.1007/s11665-020-05221-x
62. B. Li, Y. Du, Z. Chu, W. Zhou, and X. Yang, Research on Dynamic Recrystallization Behavior of Ni[sbnd]Fe[sbnd]Cr Based Alloy, *Mater Charact*, 2020, **169**, p 110653. https://doi.org/10.1016/j.matchar.2020.110653
63. C. Sun, Y. Xiang, Q. Zhou, D.J. Politis, Z. Sun, and M. Wang, Dynamic Recrystallization and Hot Workability of 316LN Stainless Steel, *Metals*, 2016, **6**(7), p 1–13. https://doi.org/10.3390/met6070152

64. A. Momeni and K. Dehghani, Hot Working Behavior of 2205 Austenite-Ferrite Duplex Stainless Steel Characterized by Constitutive Equations and Processing Maps, *Mater. Sci. Eng. A*, 2011 https://doi.org/10.1016/j.msea.2010.11.020
65. Y. Sen Hao, W.C. Liu, and Z.Y. Liu, Microstructure Evolution and Strain-Dependent Constitutive Modeling to Predict the Flow Behavior of 20Cr–24Ni–6Mo Super-Austenitic Stainless Steel During Hot Deformation, *Acta Metall. Sin.*, 2018, **31**(4), p 401–414. https://doi.org/10.1007/s40195-017-0657-5
66. M.O. Bodunrin, L.H. Chown, J.W. van der Merwe, and K.K. Alaneme, Hot Working of Ti-6Al-4V with a Complex Initial Microstructure, *Int. J. Mater. Form.*, 2019, **12**(5), p 857–874. https://doi.org/10.1007/s12289-018-1457-9
67. Y. Peng et al., Dynamic Recrystallization Behavior of Low-Carbon Steel During Hot Rolling Process: Modeling and Simulation, *J. Mater. Res. Technol.*, 2022, **20**, p 1266–1290. https://doi.org/10.1016/j.jmrt.2022.07.039
68. M. Hu, L. Dong, Z. Zhang, X. Lei, R. Yang, and Y. Sha, Correction of Flow Curves and Constitutive Modelling of a Ti-6AL-4V Alloy, *Metals*, 2018, **8**(4), p 1–15. https://doi.org/10.3390/met8040256
69. A. Hadadzadeh and M.A. Wells, Analysis of the Hot Deformation of ZK60 Magnesium Alloy, *J. Magnes. Alloy.*, 2017, **5**(4), p 369–387. https://doi.org/10.1016/j.jma.2017.09.002
70. J. Zhang, H. Di, X. Wang, Y. Cao, J. Zhang, and T. Ma, Constitutive Analysis of the Hot Deformation Behavior of Fe-23Mn-2Al-0.2C Twinning Induced Plasticity Steel in Consideration of Strain, *Mater. Des.*, 2013, **44**, p 354–364. https://doi.org/10.1016/j.matdes.2012.08.004
71. Y.P. Li, H. Matsumoto, and A. Chiba, Correcting the Stress-Strain Curve in the Stroke-Rate Controlling Forging Process, *Metall. Mater. Trans. A Phys. Metall. Mater. Sci.*, 2009, **40**(5), p 1203–1209. https://doi.org/10.1007/s11661-009-9811-7
72. L.Y. Qian, G. Fang, P. Zeng, and L.X. Wang, Correction of Flow Stress and Determination of Constitutive Constants for Hot Working of API X100 Pipeline Steel, *Int. J. Press. Vessel. Pip.*, 2015, **132–133**, p 43–51. https://doi.org/10.1016/j.ijpvp.2015.05.008
73. H. Wang, G. Qin, and C. Li, A Modified Arrhenius Constitutive Model of 2219-O Aluminum Alloy Based on Hot Compression with Simulation Verification, *J. Mater. Res. Technol.*, 2022, **19**, p 3302–3320. https://doi.org/10.1016/j.jmrt.2022.06.080
74. B. Adam, J. Tucker, and G. Tewksbury, Hot Deformation Data for Haynes 214, Haynes 230 and Inconel 740H, *Data Br.*, 2020, **28**, p 104923. https://doi.org/10.1016/j.dib.2019.104923
75. A. Tabei, F.H. Abed, G.Z. Voyiadjis, and H. Garmestani, Constitutive Modeling of Ti-6Al-4V at a Wide Range of Temperatures and Strain Rates, *Eur. J. Mech. A/Solids*, 2017, **63**, p 128–135. https://doi.org/10.1016/j.euromechsol.2017.01.005
76. L.F. Kanan, B. Vicharapu, D.R. Pissanti, C.E.F. Kwietniewski, T. Clarke, and A. De, An Investigation on Girth Friction Welding of Duplex Stainless Steel Pipes, *J. Manuf. Process.*, 2020, **51**, p 73–82. https://doi.org/10.1016/j.jmapro.2020.01.032
77. K.K. Saxena, V. Pancholi, S.K. Jha, G.P. Chaudhari, D. Srivastava, and G.K. Dey, A Novel Approach to Understand the Deformation Behavior in Two Phase Region Using Processing Map, *J. Alloys Compd.*, 2017, **706**, p 511–519. https://doi.org/10.1016/j.jallcom.2017.02.177
78. L.X. Li, Y. Lou, L.B. Yang, D.S. Peng, and K.P. Rao, Flow Stress Behavior and Deformation Characteristics of Ti-3Al-5V-5Mo Compressed at Elevated Temperatures, *Mater. Des.*, 2002, **23**(5), p 451–457. https://doi.org/10.1016/S0261-3069(02)00025-0
79. T. R. Society, P. Transactions, R. Society, P. Sciences, Recovery and Recrystallization by Stacking Fault
80. H. Zhao, J. Qi, G. Liu, R. Su, and Z. Sun, A Comparative Study on Hot Deformation Behaviours of Low-Carbon and Medium-Carbon Vanadium Microalloyed Steels, *J. Mater. Res. Technol.*, 2020, **9**(5), p 11319–11331. https://doi.org/10.1016/j.jmrt.2020.08.016
81. X. Wang, Z. Liu, and H. Luo, Complicated Interaction of Dynamic Recrystallization and Precipitation During Hot Deformation of Ultrahigh-Strength Stainless Steel, *Metall. Mater. Trans. A Phys. Metall. Mater. Sci.*, 2016, **47**(12), p 6248–6258. https://doi.org/10.1007/s11661-016-3743-9
82. A. Momeni, K. Dehghani, and X.X. Zhang, Mechanical and Microstructural Analysis of 2205 Duplex Stainless Steel Under Hot Working Condition, *J. Mater. Sci.*, 2012, **47**(6), p 2966–2974. https://doi.org/10.1007/s10853-011-6130-3
83. G.G. Yapici, I. Karaman, and Z.P. Luo, Mechanical twinning and texture evolution in severely deformed Ti-6Al-4V at high temperatures, *Acta Mater.*, 2006, **54**(14), p 3755–3771. https://doi.org/10.1016/j.actamat.2006.04.007